Science

AAAS

Supplementary Materials for

Atmospheric waves and global seismoacoustic observations of the January 2022 Hunga eruption, Tonga

Robin S. Matoza *et al*.

Corresponding author: Robin S. Matoza, rmatoza@ucsb.edu

Science **377**, 95 (2022)
DOI: 10.1126/science.abo7063

The PDF file includes:

Materials and Methods
Supplementary Text
Figs. S1 to S30
Tables S1 to S3 and S5
References

Other Supplementary Material for this manuscript includes the following:

Table S4
Movies S1 to S7
Data S1 to S8

Contents

S1. Materials and Methods

S2. Supplementary Text

S3. Figures

S4. Tables

S5. Movies

S6. Data

S7. References and Notes

S1. Materials and Methods

S1.1. Sensor response removal

Pressure sensor (barometer, microbarometer, and infrasound) response removal is primarily performed by deconvolving the instrument response in the frequency domain using ObsPy *(29)*. Due to the extremely long periods of some of the atmospheric waves from the Hunga eruption (>3000 s), which is beyond the flat portion of many of the sensor response curves (Fig. S1), care must be taken to account for the full frequency response and associated uncertainties. For the microbarometer and infrasound sensor response removal, we apply a cosine-tapered bandpass filter between 10,000 s and the Nyquist frequency to reduce overamplification during deconvolution. Barometer response removal is performed using a polynomial response function, which is simply a time-domain linear mapping from counts to Pascals (Pa). We detrend barometer data using a linear trend to focus on pressure changes rather than absolute pressure amplitudes.

The overlap in flat passband between the barometer and microbarometer (Fig. S1) sensor responses facilitates wideband analysis of the Hunga pressure waves (Fig. 2,3), as well as quality checks on derived signals. We note that Lamb wave amplitudes derived from the Hyperion IFS-5113 and IFS-5313 sensors at IMS infrasound stations showed a systematic underestimation to other data, including co-located barometers, and therefore we did not include Lamb wave amplitudes from these sensors in our analysis. We suggest the somewhat sharper roll-off of these sensors at very low frequencies and uncertainty in the factory calibrations (Fig. S1, <0.1 mHz) may be responsible for the disagreement, and again stress the need for careful examination of signals well outside the flat passband of the instruments.

S1.2. Barometer, infrasound, and seismic record sections (Fig. 2B-D)

The seismic, infrasound, and barometer data were mostly downloaded from public FDSN web services using the ObsPy "MassDownloader" library *(29)*. See Materials and Methods 17 for a full list of network codes. A handful of additional traces have been added manually. Raw, 6 day-long waveforms were stored locally for further processing. The preprocessing for each unique SEED ID included merging (interpolating short gaps), rejecting traces with large (> 10 min gaps), demeaning, and tapering with 500 seconds on both sides. A bandpass filter was applied to all traces, depending on their original sampling frequency and type: 0.0001 to 0.02 Hz for the LD channels *(30)*, 0.0001 to 2.0 Hz for the BD channels and finally 0.0001 to 1.0 Hz for the seismic channels. Traces were further downsampled to 10 s, 4 Hz or 2 Hz, for LD, BD or seismic channels, respectively. Preprocessed traces were saved to disk for further processing. All traces were visually checked to assess general quality (e.g., clear arrivals, good signal-to-noise ratio, absence of large data gaps) and low-quality traces were rejected.

Fig. 2B is computed by re-reading preprocessed LD and BD channels and bandpass-refiltering them between 0.0001 and 0.001 Hz. Fig. 2C uses BD channels refiltered between 0.01 and 2 Hz, while Fig. 2D uses vertical seismic channels (BHZ, HHZ, EHZ, SHZ, LHZ, or VHZ) between 0.01 and 0.05 Hz. The BD and seismic channels are further processed to compute the envelope of the signals. Filtered traces are aggregated (averaged) by radial distance from Hunga volcano, with a bin size of 100 km for infrasound data, and 50 km for seismic data (see Fig. S7 for details on the number of stations aggregated in each bin). The sections are finally plotted by sorting the aggregated traces by distance, as waveforms (Fig. 2B), envelopes (Fig. 2C), or as color-coded amplitudes (Fig. 2D) to enhance readability.

S1.3. Arrival time comparison for Krakatau 1883 and Hunga 2022 (Fig. 2A)

Arrival time information for the Krakatau 1883 eruption signals recorded on barometers is from Tables 3 and 4 in (*12*). These tables include up to 7 arrivals (4 + 3 antipodal) for 44 stations globally.

For the seven-day period beginning 2022-01-15 00:00:00 to 2022-01-22 00:00:00, 43 of the 53 certified IMS infrasound array stations had complete waveform data (no gaps) for at least one BDF channel per station. To recover the Hunga 2022 low-frequency Lamb wave pulse, and to allow a direct comparison with the Krakatau barometer arrival time picks (Fig. 2A), the microbarometer response was deconvolved from the IMS data. To reduce long-period noise amplification, a bandpass filter was applied with a response of one between 9.26e-5 and 5 Hz and cosine tapered to zero at 4.63e-5 and 9 Hz. No additional filtering was undertaken. The time of the signal maximum amplitude was then manually picked for each arrival.

It has been shown that waves from the eruption traveled several cycles around the Earth. We reviewed low frequency Lamb waves recorded on barometers (channel; LDO, 1 Hz) deployed as part of the Global Seismographic Network (GSN). We estimated arrival times (Fig. 2A) and amplitudes (Fig. 2F) from the waveforms for 140 hours after the origin time based on a short term average/long term average (STA/LTA) detection trigger automatically scanning the waveforms within the celerity range from 0.35 to 0.25 km/s. Trigger parameters (i.e. STA window) were tuned based on the signal duration and shape. An LTA window was set to time based on the celerity range for each station. The detection trigger threshold was set to 0.7 times the average of STA/LTA. The detection results were reviewed with adjustment to starting and ending times as needed, and the removal of outliers. We estimated arrival times (pick of maximum amplitude peak), and the peak-to-peak amplitudes of the detected signals. The frequency band from 1/10800 to 1/360 Hz was used in Lamb wave amplitude analysis in order to capture the low-frequency energy and compare with the historical dataset. Global peak-to-peak amplitude and arrival time estimates for the Hunga 2022 signal are provides in Data S7 and S8, respectively.

S1.4. Waveform comparison for Krakatau 1883 and Hunga 2022 (Fig. 2A, Fig. S8)

Zoomed in waveforms from (*12*) were digitized using WebPlotDigitizer (*31*) but no amplitude or time information is evident in the text. There was one station (Aberdeen) that had amplitude information listed in the table of (*11*) for the same arrival that was used to calibrate the pressure amplitude in Fig. S8A,C. The same waveform for the Aberdeen A1 arrival from (*12*) is also included in a figure in (*11*), though the signal to noise ratio of the figure is much lower. The waveform in (*11*) with a known time axis was digitized and used to calibrate the time axis from the higher quality (*12*) waveform. This is done for both the A1 and A2 arrivals at the Aberdeen station.

The comparison for the A1 arrival at Aberdeen for Krakatau 1883 with the A1 arrival at Reading for Hunga 2022 is shown as an inset in Fig. 2A as well as Fig. S8A,B and the A2 arrivals are shown in Fig. S8C,D. The digitized and uncalibrated waveform for the A1 arrival of the Krakatau 1883 eruption at South Georgia (*12*) is compared with the A1 arrival of the Hunga 2022 eruption at King Edward Point (South Georgia) in Fig. S8E,F.

Digitized waveforms for Aberdeen A1/A2 and South Georgia A1 from (*12*) are included as Data S1 - Data S3. Reading data for the Hunga 2022 are published in (*32*) and can be accessed at https://doi.org/10.17864/1947.000354 (*33*). King Edward Point (South Georgia) data for the Hunga 2022 eruption are provided by the British Antarctic Survey (BAS) and included as Data S4.

S1.5. Nonlinear acoustic propagation as the cause for audible sound in Alaska

The Kenai, Alaska (AV network, station KENI, channel 1) station spectrogram in Fig. 3E, with a high sampling rate of 100 Hz, shows clearly the 30-minute time period (approximately 13:15 - 13:45) during which the Hunga eruption was audible. The spectrogram was made using a 20 sec window length and 50% overlap, and the PSD was constructed with 100 s windows and 50% overlap. From that spectrogram, the two spectra shown in the middle panel (0.01 Hz frequency resolution) reveal the pre-eruption ambient baseline (Noise) as well as the time period with the maximum energy at 40 Hz (Peak, 13:34 - 13:48). This power spectral density (PSD) has a distinct spectral shape that reveals that nonlinear acoustic propagation is the cause of the audibility. For sufficiently low absorption, propagating noise undergoes nonlinear distortion, causing energy to cascade to higher frequencies as shocks form. Shock-containing noise takes on a characteristic spectral shape (f^{-2}, or -20 dB/decade high-frequency slope), identified as the "Ideal Shock" line in the middle panel of Fig. 3E. Propagating shocks maintain this slope up to a frequency corresponding to the characteristic inverse rise-time of the shocks (~5 Hz in Fig. 3E), beyond which a faster spectral exponential roll-off occurs (34). As the propagating waveform amplitude is reduced, and shock fronts gradually thicken in what is referred to as the shock "old-age" regime, the frequency at which the ideal-shock slope is replaced by the exponential roll-off lessens. Nonetheless, these shocks are visible in the waveform, as evidenced by high-amplitude (~90-103 dB peak SPL) impulses in the bottom panel of Fig. 3E that are emphasized by filtering the waveform with a two pole acausal Butterworth filter between 10 and 40 Hz.

S1.6. Global spectral analysis of seismic and pressure data

Power spectral densities (PSD) of seismic and pressure data are computed using the sine multi-tapers code developed by Robert L. Parker (35). A six-hour window containing the Lamb wave is selected at each of the 1296 seismic (LHZ) and 134 pressure (LDO) stations worldwide. Then we perform coherence analysis for 66 co-located pressure and seismic sensors. Data with gaps are discarded and the average PSDs and coherence are displayed in Fig. 3C. Selected stations have distances to the eruption between 6.7° and 177.6°. To convert the PSDs into decibels (dB), we use a reference pressure and seismic velocity of 20 µPa and 1 m/s, respectively.

S1.7. Pressure and seismic at MSVF (Fig. S25).

In forming the spectra (Fig. S25B), we perform the following processing steps. We take a 26-hour window of data starting at the eruption time of 04:14:45 on 15 January 2022. We then perform a linear detrend of the data before zero-filling any data gaps. Next, we apply a Kaiser window with a side-lobe tradeoff of 2 to the data before zero-padding to 36.4 hours (2^{17} samples). Finally, we calculate the spectra for both pressure and seismic data and remove the nominal response through spectral division.

S1.8. Himawari 8, GOES 16 & 17, Meteosat 8 & 11

Himawari 8, GOES 16 & 17, and Meteosat 8 & 11 are meteorological satellites located at around 35800 km above the equator on the geostationary orbit. Himawari 8 is owned and operated by the Japan Meteorological Agency (JMA) and is located at longitude 140.7°E in order to provide constant and uniform coverage of east Asia, and the western and central Pacific regions. GOES 16 & 17 are owned and operated by the National Oceanic and Atmospheric Administration (NOAA),

the former is located at 75°W and the latter at 137.2°W providing coverage of the Americas and the Pacific Ocean. Meteosat 8 & 11 are owned and operated by Eumetsat (European Organisation for the Exploitation of Meteorological Satellite) and are located at longitude 0° and 41.5°E providing coverage of Europe, Africa, and the Indian Ocean.

The main instrument onboard Himawari-8, the Advanced Himawari Imager (AHI), is a 16-channel multispectral imager with a nominal resolution at nadir of 2 km and a temporal resolution of 10 minutes. This instrument is similar to the Advanced Baseline Imager (ABI) onboard GOES 16 & 17 who provide the same spatio-temporal resolution. Onboard Meteosat-11 is the Spinning Enhanced Visible and Infra-Red Imager (SEVIRI) radiometer, which is a 12-channel multispectral imager with spatial resolution at nadir of 3 km and a temporal resolution of 15 minutes. They all operate in the visible and thermal infrared domain and are primarily dedicated to the observations of the Earth's atmosphere, clouds, land, and sea surfaces with applications in nowcasting and numerical weather prediction. These observations at the top of the atmosphere are driven by the molecular absorption of the electromagnetic spectrum, the scattering of light by the atmospheric particles (clouds and aerosols) as well as by the surface contribution.

Observations from Himawari-8, GOES 16 & 17 data are freely available and can be downloaded from the Amazon Web Service. Meteosat 8 & 11 observations are freely available through the Eumetsat Earth's Observation portal (https://eoportal.eumetsat.int/).

S1.9. Geostationary weather satellites and brightness temperature variations

Fig. 4A as well as Movie S 2 were made from Himawari-8 observations, Movie S 3 and Movie S 4 were made from GOES 17 & 16 observations, and Movie S 5 and Movie S 6 were made from Meteosat 8 & 11 observations. Each snapshot has been computed as the difference between instantaneous snapshots and a moving average of 3 snapshots (covering a period of 30 minutes for AHI and ABI, and a period of 45 minutes for SEVIRI); the slow moving cloud effect is therefore mitigated in comparison to the fast moving Lamb wave perturbation. Acoustic-gravity waves emanating from the eruption are also clearly visible on the images. Similar observations made using a sun-synchronous low-earth-orbit by NOAA-10 weather satellite during the Pinatubo volcanic eruption were reported by (36). We applied this procedure to Infrared channels of the Himawari-8, GOES 16 & 17 as well as Meteosat 8 & 11 observations. The Lamb wave and the following waves are all clearly visible on all infrared channels. We presented the 6.2 µm channel, which is a water vapor absorbing channel whose sensitivity peaks at around 350 hPa, corresponding to the high troposphere (~8 km) according to their weighting functions (*cf*. Fig. S5). This emphasizes the ground-atmosphere coupling of the wave propagation.

S1.10. Radio occultations

The radio occultation (RO) technique tracks GNSS signals transmitted from multiple navigation constellations (*e.g.*, GPS, GLONASS, Galileo) from a receiver located on low Earth orbiters (LEOs) on the opposite side of the Earth's limb. As the carrier signal traverses through the Earth's atmosphere, it experiences refraction due to the Earth's vertically varying atmosphere. Phase measurements provide atmospheric air density, pressure, refractive index, and temperature information (37). The relative motion of the GNSS-LEO satellite pairs allows for the vertical scanning of the Earth's atmosphere, from the surface up to ~600 km, providing both the vertical

distribution of the neutral atmospheric and the ionospheric states over random locations based on the transmitter-receiver geometry (*38*).

In Fig. 4, the RO-I profile is obtained from the COSMIC-2 constellation (*39*), while both the RO-II and RO-III profiles are obtained from the Spire constellation (*40*).

S1.11. GNSS Data and JPL's Global Differential GPS (GDGPS) Network

JPL's GDGPS network collects raw carrier-phase data from a set of stations (Materials and Methods S1.15) in real time, over Internet Protocol, at the highest possible rate of one sample per second. A first pre-processing step flags disjointed arcs and levels the carrier-phase data using the pseudorange observations (*41*). Multi-GNSS orbits are also collected in real time, though at a lower rate, and are subsequently interpolated to obtain Ionospheric Pierce Points (IPPs, see Materials and Methods S1.13) at the desired rate.

The GDGPS network collects ground receiver data from multiple sources: the publicly available International GNSS Service (IGS), the NASA Global GNSS Network, and GDGPS-owned stations. In this manuscript, a total of 71 stations from the GDGPS network were used to produce the TEC time series. Most of those stations keep track of the four main GNSS satellite constellations: BeiDou, Galileo, GLONASS, and GPS.

In Fig. 4C, the GNSS link G-I is between Centre National d'Etudes Spatiales (CNES) station FTNA and Galileo satellite E212, and G-II is between Geoscience Australia station TOW2 and Galileo satellite E212. In Fig. 4E, the hodochron is composed of a total 5778 satellite-station links. In Fig. 4F, the GNSS link G-III is between Geoscience Australia station TUVA and quasi-geostationary QZSS satellite J01.

S1.12. Total Electron Content (TEC)

The Total Electron Content (TEC) is the 3D integral of the electronic density within a 1-meter-diameter cylinder along the line of sight between a satellite and a ground receiver and is often expressed in "TEC Units" (TECU), where 1 TECU = 10^{16} electrons/m^2. The carrier phase delay between two GNSS radio signals is driven by the integral of the signals' refractive index along the line of sight (*42*, Eq. (6.83)). The line-of-sight slant TEC (STEC) can be obtained using the Appleton-Hartree formula (*42*, Eq. (6.72)):

$$\text{STEC} \simeq \frac{f_1^2 f_2^2}{K(f_1^2 - f_2^2)} (\phi_1 - \phi_2),$$

where $f_{1,2}$ are the two different carrier frequencies, $\phi_{1,2}$ are the measured phases along the respective frequencies. K is a constant derived from the plasma frequency (*42*, Eq. (39.3)):

$$K = \frac{1}{2} \frac{q_e^2}{4\pi^2 \varepsilon_0 m_e} \simeq 40.308 \text{ m}^3\text{s}^{-2},$$

where q_e is the charge of the electron, m_e is the mass of the electron, and ε_0 is the dielectric constant of a vacuum.

In Fig. 4E, the TEC is computed from 1-Hz sampled GDGPS data using JPL's proprietary software GNSS-TEC, and detrended using polynomials, the degree of which is optimized to minimize the R^2 score of the detrending. In Fig. 4C, links G-I and G-II follow the same processing steps, with an additional high-pass filtering with a cut-off period of 1 hour. In Fig. 4F, the TEC for link G-III is computed from 30-second sampled data using a Python software (https://github.com/gnss-lab/gnss-tec); we detrend the resulting uncalibrated TEC using a degree

10 polynomial and perform bandpass-filtering between 0.7 and 3 mHz (periods from 6 to 24 minutes).

S1.13. Ionospheric Pierce Point (IPP)

Since most of the electron content is concentrated in a small region of the atmosphere, it is customary to associate the measured TEC value to a single point in space. For a given satellite-station link, the Ionospheric Pierce Point (IPP) is defined as the intersection of the line of sight (linking satellite to station) with a predefined "ionospheric thin shell." Throughout this manuscript, the ionospheric shell was chosen at 450 km. Note that since GNSS satellites move with time, the IPP associated with a link moves as well, effectively measuring the TEC over different spatio-temporal points.

S1.14. Tsunamimeters – Sea level height

Sea-level data are derived from DART buoy ocean bottom pressure sensors designed for tsunami wave detection assuming the hydrostatic hypothesis (*43*). The data are accessible in text format from the NDBC/NOAA website (https://www.ndbc.noaa.gov/).

S1.15. Data availability

- Most seismic, infrasound and barogram data are available from FDSN and EIDA nodes (e.g. IRIS, http://www.iris.edu/ and http://www.orfeus-eu.org/data/eida/nodes/). See the list of network codes in Methods and Materials S1.16.
- Data from Singapore (Infrasound), New Zealand (Barometric) and Mexico (Seismic and Infrasound) can be found under the following repository: https://researchdata.ntu.edu.sg/dataset.xhtml?persistentId=doi:10.21979/N9/T9MXZY&version=DRAFT
- KIGAM seismic data are acquired by the KG network. Infrasound data used in this study are recorded at the Korea Infrasound Network operated by KIGAM. Data can be found under the following repository: https://researchdata.ntu.edu.sg/dataset.xhtml?persistentId=doi:10.21979/N9/T9MXZY&version=DRAFT
- KMA seismic and barogram data are available from https://necis.kma.go.kr/ and https://data.kma.go.kr/, respectively.
- Seismic and infrasound data from the Netherlands Seismic and Acoustic network are available through http://rdsa.knmi.nl/. Barometric data are available through https://dataplatform.knmi.nl/
- Data from Italy (Infrasound) can be found under the following repository https://doi.org/10.17605/OSF.IO/NJB8R
- Data from Ecuador (Infrasound) are available from Descarga de Señales de Infrasonido - Instituto Geofísico - EPN, https://www.igepn.edu.ec/senales-sismicas/fomulario-infrasonido
- Barometer data from the Tonga tide station were collected by the Climate and Oceans Support Program in the Pacific (COSPPac) project, an Australian Aid project, and made available by the Australian Bureau of Meteorology. Data could be found under the following repository:

- https://researchdata.ntu.edu.sg/dataset.xhtml?persistentId=doi:10.21979/N9/T9MXZY&version=DRAFT
- Barogram data from the Reading station can be accessed at https://doi.org/10.17864/1947.000354
- International Monitoring System (IMS) data are freely available on the virtual Data Exploitation Centre (vDEC) through a contract for limited access to IMS data and International Data Center (IDC) products of the Preparatory commission for the Comprehensive nuclear-Test-Ban Treaty Organization (CTBTO) for scientific project purposes (https://www.ctbto.org/specials/vdec/).
- We thank the waveform analysts of the IDC for their timely analysis of the event, the IMS and IDC for ensuring timely availability of high quality data, and all station operators of IMS facilities for the high rate of availability of high quality data.
- S-net data are available from National Research Institute for Earth Science and Disaster Resilience (https://doi.org/10.17598/nied.0007), DART data are available from NOAA (https://www.ngdc.noaa.gov/hazard/DARTData.shtml), tide gauge data at Kamaishi are available from Hydrographic and Oceanographic Department of Japan Coast Guard (https://www1.kaiho.mlit.go.jp/jhd-E.html), and tide gauge data at Kushiro are available from Japan Meteorological Agency (https://www.jma.go.jp/jma/indexe.html).
- Sea level height data are accessible in text format from the NDBC/NOAA website (https://www.ndbc.noaa.gov/).
- Observations from Himawari-8, GOES 16 & 17 data are freely available and can be downloaded from the Amazon Web Service. Meteosat 8 & 11 observations are freely available through the Eumetsat Earth's Observation portal (https://eoportal.eumetsat.int/).
- GNSS Data and JPL's Global Differential GPS (GDGPS) Network: The 1 Hz data are available by request to JPL's GDGPS service (https://ga.gdgps.net/). For the stations in the IGS network, 30-seconds data are available through the IGS' servers:
  - https://cddis.nasa.gov
  - https://geodesy.noaa.gov/corsdata/
  - https://igs.bkg.bund.de/root_ftp
  - ftp://data-out.unavco.org
  - ftp://ftp.sonel.org
  - ftp://ftp.data.gnss.ga.gov.au
  - ftp://ftp.geonet.org.nz
  - ftp://garner.ucsd.edu
  - ftp://igs.ign.fr
  - ftp://igs.bkg.bund.de
  - ftp://geoftp.ibge.gov.br
  - ftp://mgmds01.tksc.jaxa.jp
  - ftp://ncedc.org

S1.16. Citations for seismo-acoustic networks used in this study

Network information for seismic, atmospheric pressure, and hydrophone networks used in this study. Network codes are listed in **bold** along with citation information as shown on the FDSN website, where available.

- **2O**: Glanville, H. (2019). Beetaloo Seismic Monitoring Project [Data set]. International Federation of Digital Seismograph Networks. https://doi.org/10.7914/SN/2O_2019

- **AF**: Penn State University. (2004). AfricaArray [Data set]. International Federation of Digital Seismograph Networks. https://doi.org/10.7914/SN/AF
- **AI**: Istituto Nazionale di Oceanografia e di Geofisica Sperimentale. (1992). Antarctic Seismographic Argentinean Italian Network - OGS [Data set]. International Federation of Digital Seismograph Networks. https://doi.org/10.7914/SN/AI
- **AK**: Alaska Earthquake Center, Univ. of Alaska Fairbanks. (1987). Alaska Regional Network [Data set]. International Federation of Digital Seismograph Networks. https://doi.org/10.7914/SN/AK
- **AM**: Raspberry Shake, S.A. (2016). Raspberry Shake [Data set]. International Federation of Digital Seismograph Networks. https://doi.org/10.7914/SN/AM
- **AT:** NOAA National Oceanic and Atmospheric Administration (USA). (1967). National Tsunami Warning Center Alaska Seismic Network [Data set]. International Federation of Digital Seismograph Networks. https://doi.org/10.7914/SN/AT
- **AU**: Geoscience Australia. Australian National Seismograph Network
- **AV**: Alaska Volcano Observatory/USGS. (1988). Alaska Volcano Observatory [Data set]. International Federation of Digital Seismograph Networks. https://doi.org/10.7914/SN/AV
- **AW**: Alfred Wegener Institute For Polar And Marine Research (AWI). (1993). AW – AWI Network Antarctica. Deutsches GeoForschungsZentrum GFZ. https://doi.org/10.14470/NJ617293
- **AZ**: UC San Diego. (1982). ANZA Regional Network [Data set]. International Federation of Digital Seismograph Networks. https://doi.org/10.7914/SN/AZ
- **BE:** Royal Observatory of Belgium. (1985). Belgian Seismic Network [Data set]. International Federation of Digital Seismograph Networks. https://doi.org/10.7914/SN/BE
- **BK**: Northern California Earthquake Data Center. (2014). Berkeley Digital Seismic Network (BDSN) [Data set]. Northern California Earthquake Data Center. https://doi.org/10.7932/BDSN
- **BL:** Universidade de Sao Paulo, USP. (1988). Brazilian Lithospheric Seismic Project (BLSP).
- **BN:** Blacknest (AWE UK). (1980). UK-Net, Blacknest Array.
- **BX:** Department of Geological Survey of Botswana. (2001). Botswana Seismological Network (BSN).
- **C:** Universidad de Chile, Dept de Geofisica. (1991). Chilean National Seismic Network
- **C1:** Universidad de Chile. (2012). Red Sismologica Nacional [Data set]. International Federation of Digital Seismograph Networks. https://doi.org/10.7914/SN/C1
- **C0**: Colorado Geological Survey. (2016). Colorado Geological Survey Seismic Network [Data set]. International Federation of Digital Seismograph Networks. https://doi.org/10.7914/SN/C0
- **CA**: Institut d'Estudis Catalans (1996): Catalan Seismic Network. International Federation of Digital Seismograph Networks. https://doi.org/10.7914/SN/CA
- **CC:** Cascades Volcano Observatory/USGS. (2001). Cascade Chain Volcano Monitoring [Data set]. International Federation of Digital Seismograph Networks. https://doi.org/10.7914/SN/CC
- **CH**: Swiss Seismological Service (SED) At ETH Zurich. (1983). National Seismic Networks of Switzerland. ETH Zürich. https://doi.org/10.12686/sed/networks/ch

- **CI**: California Institute of Technology and United States Geological Survey Pasadena. (1926). Southern California Seismic Network [Data set]. International Federation of Digital Seismograph Networks. https://doi.org/10.7914/SN/CI
- **CM**: INGEOMINAS - Servicio Geológico Colombiano (SGC Colombia). (1993). Red Sismológica Nacional de Colombia [Data set]. International Federation of Digital Seismograph Networks. https://doi.org/10.7914/SN/CM
- **CN**: Geological Survey of Canada. (1989). Canadian National Seismograph Network [Data set]. International Federation of Digital Seismograph Networks. https://doi.org/10.7914/SN/CN
- **CP**: CIVISA - Centro de Informação e Vigilância Sismovulcânica dos Açores (CIVISA) University of Azores. (2008). CIVISA Seismo-Volcanic Monitoring Network-Azores Islands.
- **CR**: University of Zagreb. (2001). Croatian Seismograph Network [Data set]. International Federation of Digital Seismograph Networks. https://doi.org/10.7914/SN/CR
- **CU**: Albuquerque Seismological Laboratory (ASL)/ U.S. Geological Survey (USGS). (2006). Caribbean USGS Network [Data set]. International Federation of Digital Seismograph Networks. https://doi.org/10.7914/SN/CU
- **CX**: GFZ German Research Centre For Geosciences, & Institut Des Sciences De L'Univers-Centre National De La Recherche CNRS-INSU. (2006). IPOC Seismic Network. Integrated Plate boundary Observatory Chile - IPOC. https://doi.org/10.14470/PK615318
- **CZ**: Charles University in Prague (Czech), Institute of Geonics, Institute of Geophysics, Academy of Sciences of the Czech Republic, Institute of Physics of the Earth Masaryk University (Czech), & Institute of Rock Structure and Mechanics. (1973). Czech Regional Seismic Network [Data set]. International Federation of Digital Seismograph Networks. https://doi.org/10.7914/SN/CZ
- **DK**: GEUS Geological Survey of Denmark and Greenland. (1976). Danish Seismological Network.
- **DR**: National Seismological Centre of Autonomous University of Santo Domingo. (1998). Centro Nacional de Sismologia [Data set]. International Federation of Digital Seismograph Networks. https://doi.org/10.7914/SN/DR
- **EE**: Geological Survey of Estonia. (1998). Estonian Seismic Network
- **EI**: Dublin Institute for Advanced Studies. (1993). Irish National Seismic Network [Data set]. International Federation of Digital Seismograph Networks. https://doi.org/10.7914/SN/EI
- **FN**: Sodankyla Geophysical Observatory / University of Oulu (Finland). (2005). Northern Finland Seismological Network.
- **FR**: RESIF. (1995). RESIF-RLBP French Broad-band network, RESIF-RAP strong motion network and other seismic stations in metropolitan France [Data set]. RESIF - Réseau Sismologique et géodésique Français. https://doi.org/10.15778/RESIF.FR
- **G**: Institut de physique du globe de Paris (IPGP), & École et Observatoire des Sciences de la Terre de Strasbourg (EOST). (1982). GEOSCOPE, French Global Network of broad band seismic stations. Institut de physique du globe de Paris (IPGP), Université de Paris. https://doi.org/10.18715/GEOSCOPE.G
- **GB**: British Geological Survey. (1970). Great Britain Seismograph Network.

- **GE**: GEOFON Data Centre. (1993). GEOFON Seismic Network. Deutsches GeoForschungsZentrum GFZ. https://doi.org/10.14470/TR560404
- **GR:** Federal Institute for Geosciences and Natural Resources. (1976). German Regional Seismic Network (GRSN). Bundesanstalt für Geowissenschaften und Rohstoffe. https://doi.org/10.25928/mbx6-hr74
- **GT**: Albuquerque Seismological Laboratory (ASL)/USGS (1993): Global Telemetered Seismograph Network (USAF/USGS). International Federation of Digital Seismograph Networks. Dataset/Seismic Network. https://doi.org/10.7914/SN/GT
- **HK**: Hong Kong Observatory. (2009). Hong Kong Seismograph Network.
- **HL**: National Observatory of Athens, Institute of Geodynamics, Athens. (1975). National Observatory of Athens Seismic Network [Data set]. International Federation of Digital Seismograph Networks. https://doi.org/10.7914/SN/HL
- **HN**: Kövesligethy Radó Seismological Observatory (Geodetic And Geophysical Institute, Research Centre For Astronomy And Earth Sciences, Hungarian Academy Of Sciences (MTA CSFK GGI KRSZO)). (2017). Hungarian National Infrasound Network. GFZ Data Services. https://doi.org/10.14470/UA114590
- **HV**: USGS Hawaiian Volcano Observatory (HVO). (1956). Hawaiian Volcano Observatory Network [Data set]. International Federation of Digital Seismograph Networks. https://doi.org/10.7914/SN/HV
- **IC**: Albuquerque Seismological Laboratory (ASL)/USGS. (1992). New China Digital Seismograph Network [Data set]. International Federation of Digital Seismograph Networks. https://doi.org/10.7914/SN/IC
- **IG**: Instituto Andaluz de Geofisica, Granada University. (1997). Southern Spain Broadband Seismic Network (Southern Spain BB)
- **II**: Scripps Institution of Oceanography. (1986). Global Seismograph Network - IRIS/IDA [Data set]. International Federation of Digital Seismograph Networks. https://doi.org/10.7914/SN/II
- **IM**: (1965). International Miscellaneous Stations (IMS).
- **IU**: Albuquerque Seismological Laboratory (ASL)/USGS. (1988). Global Seismograph Network - IRIS/USGS [Data set]. International Federation of Digital Seismograph Networks. https://doi.org/10.7914/SN/IU
- **IW**: Albuquerque Seismological Laboratory (ASL)/USGS. (2003). Intermountain West Seismic Network [Data set]. International Federation of Digital Seismograph Networks. https://doi.org/10.7914/SN/IW
- **JP**: JMA Japan Meteorological Agency. (1994). Japan Meteorological Agency Seismic Network
- **KC**: Central Asian Institute for Applied Geosciences. (2008). Central Asian Seismic Network of CAIAG [Data set]. International Federation of Digital Seismograph Networks. https://doi.org/10.7914/SN/KC
- **KG**: Korean Institute of Geology, Mining and Materials. (1997). Korean Seismic Network – KIGAM
- **KO**: Kandilli Observatory And Earthquake Research Institute, Boğaziçi University. (1971). Bogazici University Kandilli Observatory And Earthquake Research Institute [Data set]. International Federation of Digital Seismograph Networks. https://doi.org/10.7914/SN/KO

- **KR**: Kyrgyz Institute of Seismology, KIS . (2007). Kyrgyz Digital Network [Data set]. International Federation of Digital Seismograph Networks. https://doi.org/10.7914/SN/KR
- **KS**: Korea Meteorological Administration, Seoul. (2006). Korea National Seismography Network (KNSN-KMA) (KNSN)
- **KZ**: KNDC/Institute of Geophysical Research (Kazakhstan). (1994). Kazakhstan Network [Data set]. International Federation of Digital Seismograph Networks. https://doi.org/10.7914/SN/KZ
- **LD**: Lamont Doherty Earth Observatory (LDEO), Columbia University. (1970). Lamont-Doherty Cooperative Seismographic Network [Data set]. International Federation of Digital Seismograph Networks. https://doi.org/10.7914/SN/LD
- **LM**: Michigan State University (MSU, Michigan USA). (2016). Michigan State University Seismic Network [Data set]. International Federation of Digital Seismograph Networks. https://doi.org/10.7914/SN/LM
- **LX**: Instituto Dom Luiz (IDL) - Faculdade de Ciências da Universidade de Lisboa. (2003). University of Lisbon Seismic Network [Data set]. International Federation of Digital Seismograph Networks. https://doi.org/10.7914/SN/LX
- **MI**: USGS Alaska Anchorage. (2000). USGS Northern Mariana Islands Network [Data set]. International Federation of Digital Seismograph Networks. https://doi.org/10.7914/SN/MI
- **MN**: MedNet Project Partner Institutions. (1990). Mediterranean Very Broadband Seismographic Network (MedNet). Istituto Nazionale di Geofisica e Vulcanologia (INGV). https://doi.org/10.13127/SD/fBBBtDtd6q
- **MS**: Meteorological Service of Singapore. (1996). Singapore Seismological Network (MS)
- **MX:** SSN (2022). Servicio Sismológico Nacional, Instituto de Geofísica, Universidad Nacional Autónoma de México, México. https://doi.org/10.21766/SSNMX/SN/MX
- **MY**: Malaysian Meteorological Service (Ministry of Science, Tech and Innovation, MOSTI-MMD-MET). (2003). Malaysian National Seismic Network
- **N4**: Albuquerque Seismological Laboratory (ASL)/USGS. (2013). Central and Eastern US Network [Data set]. International Federation of Digital Seismograph Networks. https://doi.org/10.7914/SN/N4
- **NC**: USGS Menlo Park. (1967). USGS Northern California Network [Data set]. International Federation of Digital Seismograph Networks. https://doi.org/10.7914/SN/NC
- **NK**: National Seismological Centre. (1978). Nepal Kathmandu [Data set]. International Federation of Digital Seismograph Networks. https://doi.org/10.7914/SN/NK
- **NL**: KNMI. (1993). Netherlands Seismic and Acoustic Network. Royal Netherlands Meteorological Institute (KNMI). https://doi.org/10.21944/e970fd34-23b9-3411-b366-e4f72877d2c5
- **NM**: CERI - University of Memphis. (1977). Cooperative New Madrid Seismic Network.
- **NO**: Norsar. (1971). NORSAR Station Network [Data set]. NORSAR. https://doi.org/10.21348/d.no.0001
- **NR**: Utrecht University (UU Netherlands). (1983). NARS [Data set]. International Federation of Digital Seismograph Networks. https://doi.org/10.7914/SN/NR

- **NU**: Instituto Nicaraguense de Estudios Territoriales (INETER). (1975). Nicaraguan Seismic Network [Data set]. International Federation of Digital Seismograph Networks. https://doi.org/10.7914/SN/NU
- **NW**: Northwestern University. (2011). Northwestern University Seismic Network.
- **NZ**: Institute of Geological & Nuclear Sciences Ltd (GNS New Zealand). (1988). New Zealand National Seismograph Network.
- **OE**: ZAMG - Zentralanstalt für Meterologie und Geodynamik. (1987). Austrian Seismic Network [Data set]. International Federation of Digital Seismograph Networks. https://doi.org/10.7914/SN/OE
- **OH**: Ohio Geological Survey. (1999). Ohio Seismic Network [Data set]. International Federation of Digital Seismograph Networks. https://doi.org/10.7914/SN/OH
- **OO**: Rutgers University. (2013). Ocean Observatories Initiative [Data set]. International Federation of Digital Seismograph Networks. https://doi.org/10.7914/SN/OO
- **PB**: UNAVCO. (2004). Plate Boundary Observatory Borehole Seismic Network (PBO)
- **PL**: Polish Academy of Sciences (PAN) Polskiej Akademii Nauk. (1990). Polish Seismological Network
- **PM**: Instituto Português do Mar e da Atmosfera, I.P. (2006). Portuguese National Seismic Network [Data set]. International Federation of Digital Seismograph Networks. https://doi.org/10.7914/SN/PM
- **PO**: Geological Survey of Canada. (2000). Portable Observatories for Lithospheric Analysis and Research Investigating Seismicity (POLARIS)
- **PR**: University of Puerto Rico. (1986). Puerto Rico Seismic Network & Puerto Rico Strong Motion Program [Data set]. International Federation of Digital Seismograph Networks. https://doi.org/10.7914/SN/PR
- **PS**: University of Tokyo, Earthquake Research Institute (Todai, ERI, Japan). (1989). Pacific21 (ERI/STA)
- **PY**: UC San Diego. (2014). Piñon Flats Observatory Array [Data set]. International Federation of Digital Seismograph Networks. https://doi.org/10.7914/SN/PY
- **RM**: Regional Integrated Multi-Hazard Early Warning System (RIMES Thailand). (2008). Regional Integrated Multi-Hazard Early Warning System [Data set]. International Federation of Digital Seismograph Networks. https://doi.org/10.7914/SN/RM
- **RN**: Ruhr Universitaet Bochum (RUB Germany). (2007). RuhrNet - Seismic Network of the Ruhr-University Bochum [Data set]. Federal Institute for Geosciences and Natural Resources (BGR, Germany). https://doi.org/10.7914/SN/RN
- **RO**: National Institute for Earth Physics (NIEP Romania). (1994). Romanian Seismic Network [Data set]. International Federation of Digital Seismograph Networks. https://doi.org/10.7914/SN/RO
- **S1:** Australian National University (ANU, Australia). (2011). Australian Seismometers in Schools [Data set]. International Federation of Digital Seismograph Networks. https://doi.org/10.7914/SN/S1
- **SB**: UC Santa Barbara. (1989). UC Santa Barbara Engineering Seismology Network [Data set]. International Federation of Digital Seismograph Networks. https://doi.org/10.7914/SN/SB
- **SC**: New Mexico Tech. (1999). New Mexico Tech Seismic Network

- **SG**: Multiple Operators. (1997). International Geodynamics and Earth Tide Service [Data set]. International Federation of Digital Seismograph Networks. https://doi.org/10.7914/SN/SG
- **SL**: Slovenian Environment Agency. (1990). Seismic Network of the Republic of Slovenia [Data set]. International Federation of Digital Seismograph Networks. https://doi.org/10.7914/SN/SL
- **SS**: (1970). Single Station.
- **SV**: Servicio Nacional de Estudios Territoriales (SNET El Salvador). (2004). Servicio Nacional de Estudios Territoriales (SNET), El Salvador (SNET-BB)
- **SX**: University of Leipzig. (2001). SXNET Saxon Seismic Network [Data set]. International Federation of Digital Seismograph Networks. https://doi.org/10.7914/SN/SX
- **TA**: IRIS Transportable Array. (2003). USArray Transportable Array [Data set]. International Federation of Digital Seismograph Networks. https://doi.org/10.7914/SN/TA
- **TC:** Universidad de Costa Rica. (2017). Red Sismológica Nacional de Costa Rica (RSN: UCR-ICE). https://doi.org/10.15517/TC
- **TH**: Institut fuer Geowissenschaften, Friedrich-Schiller-Universitaet Jena. (2009). Thüringer Seismologisches Netz [Data set]. International Federation of Digital Seismograph Networks. https://doi.org/10.7914/SN/TH
- **TW**: Academia Sinica, Institute of Earth Sciences. (1994). Broadband Array in Taiwan for Seismology [Data set]. International Federation of Digital Seismograph Networks. https://doi.org/10.7914/SN/TW
- **TX**: Bureau of Economic Geology, The University of Texas at Austin. (2016). Texas Seismological Network [Data set]. International Federation of Digital Seismograph Networks. https://doi.org/10.7914/SN/TX
- **UO**: University of Oregon. (1990). Pacific Northwest Seismic Network - University of Oregon [Data set]. International Federation of Digital Seismograph Networks. https://doi.org/10.7914/SN/UO
- **US**: Albuquerque Seismological Laboratory (ASL)/USGS. (1990). United States National Seismic Network [Data set]. International Federation of Digital Seismograph Networks. https://doi.org/10.7914/SN/US
- **UU**: University of Utah. (1962). University of Utah Regional Seismic Network [Data set]. International Federation of Digital Seismograph Networks. https://doi.org/10.7914/SN/UU
- **UW**: University of Washington. (1963). Pacific Northwest Seismic Network - University of Washington [Data set]. International Federation of Digital Seismograph Networks. https://doi.org/10.7914/SN/UW
- **WI**: Institut de physique du globe de Paris (IPGP). (2008). GNSS, seismic broadband and strong motion permanent networks in West Indies. Institut de physique du globe de Paris (IPGP), Université de Paris. https://doi.org/10.18715/antilles.WI
- **WM**: San Fernando Royal Naval Observatory (ROA), Universidad Complutense De Madrid (UCM), Helmholtz-Zentrum Potsdam Deutsches GeoForschungsZentrum (GFZ), Universidade De Evora (UEVORA, Portugal), & Institute Scientifique Of RABAT (ISRABAT, Morocco). (1996). The Western Mediterranean BB seismic Network. Deutsches GeoForschungsZentrum GFZ. https://doi.org/10.14470/JZ581150

- **WY**: University of Utah. (1983). Yellowstone National Park Seismograph Network [Data set]. International Federation of Digital Seismograph Networks. https://doi.org/10.7914/SN/WY
- **YN**: Vernon, F. and BenZion, Y. (2010). San Jacinto Fault Zone Experiment [Data set]. International Federation of Digital Seismograph Networks. https://doi.org/10.7914/SN/YN_2010
- **YW**: Glanville, H. (2021). Muswellbrook [Data set]. International Federation of Digital Seismograph Networks. https://doi.org/10.7914/SN/YW_2021

S2. Supplementary Text

S2.1. IMS arrays

The Provisional Technical Secretariat of the Comprehensive Nuclear-Test-Ban Treaty Organization (CTBTO) operates the IMS, a worldwide network of multi-technology monitoring stations helping to verify compliance with the Comprehensive Nuclear-Test-Ban Treaty (CTBT). The IMS infrasound network currently comprises 53 microbarometer arrays (*44*), all of which recorded signals generated by the Hunga eruption. The majority of the IMS atmospheric pressure datastreams are recorded on microbarometers for which the responses are equivalent to a high-pass filter with corner frequencies of a few mHz (see CEA-DASE and Hyperion sensor responses in Fig. S1, and the Methods and Materials S1.1 section for a discussion of response deconvolution).

The CTBTO International Data Centre (IDC) utilizes signal detections from the three waveform technologies, seismic, hydroacoustic and infrasound, to form automatic events. These are reviewed by human analysts to produce the Reviewed Event Bulletin (REB) (*45*), results of which contain the Hunga activity chronology (Fig. 1B). The REB for this event are included as Supplemental files Data S5 and Data S6.

Microbarometer arrays are used to distinguish acoustic signals of interest from noise (both acoustic and non-acoustic) and to estimate the horizontal and vertical incidence angles of the passing wavefront.

For purposes of this study, a delay-and-sum beamformer technique, e.g., (*46*), has been applied to all 53 IMS infrasound arrays. These provide us with the back-azimuth (opposite to the direction of arrival), apparent-velocity (a measure of the wave's inclination angle) and improve signal-to-noise ratio (SNR) by increasing the amplitudes of coherent signals and suppressing incoherent background noise. This analysis shows that the network recorded at least two direct and two antipodal infrasonic wave arrivals from the main explosive event. Fig. S15 shows array analyses for four IMS arrays to the west and east of Hunga volcano, following the first passage of the Lamb wave; coherent infrasound is detected for several hours. Infrasound group velocities are centered on approximately 290 m/s for stations to the west of Hunga while group velocities at stations east of Hunga are centered on approximately 250 m/s. These values correspond to typical group speeds for stratospheric and thermospheric waveguides and are consistent with expected propagation conditions on this hemisphere during this time of year.

S2.2. December 2021 to January 2022 eruption chronology

The first eruption of the December 2021 eruptive phase occurred on 19 December 2021 (mb 3.8 at 20:33 UTC, infrasound event at 20:46 UTC), detected by 12 IMS infrasound arrays. The closest IMS infrasound array IS22, located 1,848 km west of Hunga volcano in a favorable propagation direction, recorded various eruptive signals until 4 January 2022 (Fig. 1B). More powerful infrasound activity resumed on 13 January 2022 (4 and 11 detecting IMS infrasound stations at 15:19 and 17:37 UTC, respectively) with amplitudes ~10 times those of the December activity. On 14 January, infrasound activity was accompanied by very-long-period seismic tremor (Fig. S2) and an increasing number of hydroacoustic T-phase detections (Fig. 1B). The complex time-series of events on 15 January started with an infrasound-only event at 03:45 UTC (4 stations), followed by a couple of seismic, hydroacoustic (see S2.3), and infrasound (S,H,I, respectively) events between 04:00 and ~04:30 UTC as reported in the REB of the IDC (Table S1).

At least 4 IMS hydroacoustic, 21 IMS infrasound, and numerous seismic stations detected the seismic event at 04:14:45 UTC (USGS origin time, IDC origin time 04:14:59 UTC, see Table Table S1). Another REB infrasound event was formed at 04:30 UTC with arrivals at all 53 IMS infrasound arrays. The criterion for REB infrasound arrival picks and the applied velocity model are not reported and may have an implication on the origin times, whereas seismic and seismoacoustic events should have well constrained origin times due to the seismic arrivals. Although most detecting IMS infrasound stations are associated with the event around 04:30 UTC, this event does not correspond to the onset of the lower-frequency Lamb wave, but rather with an arrival that has a celerity of ~0.29 km/s for the nearest stations (i.e., IS22, IS36, IS40, IS05).

After intermittent seismic events, a last explosive eruption at ~08:31 UTC was detected by at least 20 IMS infrasound arrays and 5 IMS hydrophone sensors (at stations HA03 and HA11). Corresponding signals recorded at IS22 had a total duration of ~21 min (opposed to 80 min around the main event), after which the subaerial volcanic activity stopped. Seismic and hydroacoustic activity continued (Fig. 1B). The last date of data considered for Figure 1B is 31 January 2022.

S2.3. Hydroacoustic observations

Two IMS hydroacoustic stations (two triplets for each station) detected hydroacoustic signals associated with the Hunga eruption. The triplet arrays are located near Wake Island, USA (station HA11, 4,800 km) and Juan Fernández Island, Chile (station HA03, 9,350 km). Array processing methods (46,47) are used to analyze the data and associate the recordings with the event.

A similar waveform pattern, observed at the two stations (two triplets for each station), provides insight into the eruption sequence. These patterns are consistent with teleseismic P-wave observations, confirming that hydroacoustic observations are associated with a P-to-T seismo-acoustic coupling process. Both stations recorded two impulsive signals separated by three minutes, followed by a 20-minute continuous signal associated with the eruption; these observations are consistent with teleseismic P-waves. Interestingly, no Rg wave is observed for the first impulsive signal. The second impulsive signal is associated with the main event at 04:14:45 UTC (USGS origin time). The signals are assumed to be coupled through seismic waves because direct paths to all arrays are blocked by bathymetry. Array processing results show that back-azimuth at HA03 points towards the volcano (Fig. S3). Since one Tonga island blocks the direct path between Hunga volcano and HA03, it is assumed that the waves undergo a seismo-acoustic coupling through the Tonga-Kermadec trench. Similarly, the Marshall Islands block the direct path between the volcano and HA11; back-azimuth at HA11 points towards the north of the volcano. Arrival times suggest that P-to-T coupling likely occurs along Niue Island steep slopes. The steep bathymetry surrounding the Hunga volcano blocks any direct path to other IMS hydrophone arrays, explaining the lack of other hydroacoustic observations. Unlike the high-amplitude Lamb and infrasound signals, the hydroacoustic signals had low amplitudes (up to 1.5 Pa), slightly above the background noise level in the 2 Hz to 13 Hz frequency band.

S2.4. Dispersion curve cartoon for different wave types

Fig. S4 shows a schematic representation of dispersion curves for gravity waves, acoustic waves as well as acoustic-gravity waves (AGW) as a function of frequency and horizontal wavenumber. The figure has been adapted from the original diagram introduced by (4). Realistic dispersion curves have been computed for the MSIS empirical model by (48).

The AGW spectrum comprises both high-frequency gravity waves and low-frequency acoustic waves. The acoustic cut-off frequency of the atmosphere and Brunt-Väisälä frequency fall within this frequency range. The Lamb wave, which appears as a straight line in the figure with a constant group speed, in reality appears as a pseudo-mode due to interaction of various gravity and acoustic modes (20).

Above 10 mHz, the influence of gravity on the propagation of AGWs becomes negligible. The inaudible sound waves between 10 mHz and 20 Hz are then called infrasound.

S2.5. Contours of arrival time of the Lamb wave

If the speed of propagation is constant, the wavefront will expand uniformly from the source, and the cycle of propagation will continue until the amplitude decays to the background noise level (49). Fig. S6A shows the contour map of Lamb wave arrival times from the Hunga eruption for 6 passages (A1, A2, A3, A4, A5, and A6). We interpolated arrival times estimated from GSN, IMS, and AK networks to make a contour and compared with the calculated arrival times at fixed celerity of 0.3 km/s. For the A1 passage, there is good agreement between observations and calculated values. The circular wavefront distorted as it traveled because the speed of propagation varied along the propagation path. As the passage number increases, there are less observations (that impact the resolution of contour) and anisotropic contours as a result of different atmospheric conditions in time and space. The RMS errors between the picked arrival and the calculated times (fixed at celerity of 0.3 km/s) are 0.3, 0.9, 1.8, 1.9, 2.9, and 2.3 for A1, A2, A3, A4, A5, and A6, respectively. This results in that arrival times that vary in time and space and deviate from a circular wavefront approximation, and makes it challenging to pick arrivals especially for later passages (A5 and A6). It was also shown that the higher passages, the more scattering of arrival times in Fig. 2A. Arrival times of Lamb waves are compared with infrasound arrival times recorded at seismometers, infrasound sensors, and barometers for A1 and A2 in Fig. S6A.

S2.6. Lamb wave observed in satellite imagery

The Lamb wave has been observed on all geostationary weather satellites (see Movie S 2 - Movie S 6). Himawari-8 and GOES 17 show the source explosion, GOES 16 and Meteosat 8 show the propagation through the globe toward the antipode, and Meteosat-11 clearly shows the focalization of the Lamb wave at the antipodal location. The Lamb wave perturbation from this channel results in a 0.2 Kelvin disturbance of the top of the atmospheric brightness temperature (Fig. S5B). To the extent of our knowledge, it is the first time a Lamb wave has been observed from weather satellites on such a large spatio-temporal extent (both geostationary and polar orbiting satellites).

S2.7. Refocusing Lamb waves

The peak-to-peak amplitudes of the first passage of the Lamb wave around the globe exhibit a significant level of scatter at distances greater than ~7500 km (Fig. S9A). Some of this scatter may be attributable to anisotropic propagation effects; the lowest amplitudes are seen at stations to the west of Hunga volcano (the direction against the predominant stratospheric winds).

In addition, although scattered, the reduction in amplitude decay with range beyond 10000 km is consistent with some refocusing of the Lamb wave as it propagates towards the antipode;

this is more easily seen by plotting the amplitudes against the expected Lamb wave circumference at the distance of the station (Fig. S9B).

S2.8. Equivalent yield

Energy releases from large volcanic eruptions have often been compared with atmospheric nuclear explosions owing to well-documented observations of large atmospheric pressure disturbances from nuclear tests (13,50,51,52). Maximum amplitudes and periods of pressure oscillation during eruptions were related to the released energy equivalent to nuclear yields. However, caution must be exercised as nuclear explosions and large volcanic eruptions have substantially different source processes. Blast waves are formed by above-ground nuclear detonations when the atmosphere surrounding the explosions is compressed following the growth of nuclear fireballs (53). While the nuclear blasts produce high pressures over a relatively short period of time by initial air compression, atmospheric pressure disturbances of volcanic eruptions can be prolonged by sustained activities such as gas release/expansion, volcanic jets, and high-altitude ash plumes (54).

Fig. S10B exhibits a theoretical nuclear shock wave in comparison with the Hunga atmospheric pressure pulse recorded in Fiji (756 km). The shock waveform is generated by the scaling law which allows the pressures from one explosion to be used to predict those from another (55). We scale the peak amplitude and positive pulse duration of the 1 kT nuclear blast (Table XI in (55)) for 1700 MT to match the peak amplitude at the observation distance. Although direct comparison is not possible as the shock waveform does not include realistic propagation effects in the atmosphere, it illustrates the nature of nuclear blast at relatively short distances from the source. For the equivalent yield which matches the peak pressure amplitude of the Hunga eruption, the nuclear pulse duration (<400 s) does not match the observed long-period pressure oscillation (> 1000 s). This long-period nature of the Hunga pressure signal likely represents temporally prolonged eruption processes.

To illustrate the difficulties of applying nuclear yield models to volcanic eruptions, we attempt yield estimation via the theoretical model presented by (14), hereafter called PP71 model. Data come from 68 barometer stations (network code, IU) within the Global Seismographic Network (GSN). We only used data recorded on barometers which have a flat frequency response over the observed Lamb wave period (0.3–10 mHz). On the other hand, microbarometers in the network have narrower-band responses with rapid roll-off below ~0.01 Hz (Fig. S1), and the low-frequency instrument response must be properly removed for the Lamb waves. The barometer data are first windowed to isolate signals traveling between 290 and 350 m/s from Hunga volcano before a simple short-term average, long-term average (STA/LTA) picker is used to mark event onsets. For consistent identification of Lamb wave characteristics, we apply a bandpass filter to the data between $0.1 - 1.0$ mHz. For each event identified, the first and second peak as well as the trough are programmatically measured. Peak-to-peak (PFPT) amplitudes and time intervals between the first and second peaks (T1,2) are then used to estimate energy release (E) (14) according to

$$E = 13 P_{FPT} \, (r_e \, sin(r/re))^{1/2} Hs \, (c \, T_{1,2})^{3/2}$$

where r_e is the radius of the Earth, r is source to receiver distance, Hs is the lower atmosphere scale height (8 km), and c is the sound speed. Regression analysis of the measurements based on the PP71 model results in inordinately large yield equivalents (~5,000 MT). These large yields are primarily a function of the long (10s of minutes) peak to peak durations (Fig. S10A, large red

diamonds), which are an order of magnitude longer than recorded signals from nuclear detonations (Fig. S10A, black symbols). The PP71 model was developed by theoretical prediction of acoustic-gravity modes from nuclear detonations (*9,14*). A point energy source was assumed with an amplitude and positive pulse duration adopted at a distance of one mile from a 1 kT nuclear detonation (*9*). Therefore, the amplitude-period-yield relationship in PP71 may not be valid when the signal amplitudes and durations are affected by unaccounted source characteristics. It should also be noted that the PP71 theoretical model was compared to microbarometer records from atmospheric nuclear tests, but those records are likely affected by the limited instrument response of the microbarometers at that time (e.g., Lamont type A and B) (Fig. S1). Caution must be taken when they are compared with long-period Lamb waves of the Hunga eruption.

An empirical relationship, often referred to as the AFTAC period-yield relationship (*56*), is also not applicable to extended eruption sources. The relationship was derived from measurements of dominant infrasonic signal periods generated by atmospheric nuclear explosions (i.e., point energy sources) with yields between 0.2 kT and 15 MT (*15*). The dominant Hunga Lamb wave signal periods (1700 – 2500 s) are over one order-of-magnitude lower than those associated with the largest (15 MT) explosion (80 s) in the original dataset (*15*). Infrasonic phase periods measured across the IMS microbarometer network are scattered, but exhibit an approximately log normal distribution with a median value of 69 s and an interquartile range of [48,99] s. A naive application of the AFTAC period-yield relationship to the Hunga signals, which should be discounted due to the differences in source characteristics, equates the 69 s period to an equivalent yield of 10 MT; the significantly smaller value than the PP71 estimated value is a reflection that the empirical AFTAC relationship is insensitive to the dominant Hunga signal frequencies.

S2.9. Secondary gravity wave arrivals

Low-frequency gravity wave (GW) modes can be excited by large volcanic eruptions (*57*). These gravity modes typically exhibit a small compression phase corresponding to the first expansion of the vent opening blast followed by a stronger longer-duration rarefaction caused by the eruption column entraining air during its ascent. The propagation of acoustic-gravity waves is highly anisotropic and is promoted by strong downwind conditions preventing gravity wave energy dissipation at higher altitudes.

On 15 January 2022, favorable wind conditions occurred towards the east and southeast of Hunga volcano (see Supplementary Text S2.13 - S2.16). Pressure records in both Australia and Antarctica (Fig. S14) show a rarefaction-dominated phase (green line) traveling at lower velocities than the initial Lamb wave perturbation (red line). This rarefaction duration suggests that air was flowing into the high temperature column for ~600 s. However, the inferred GW phase velocity is close to 0.28 km/s which is significantly larger than previous near-field observations (<< 50 m/s, *57*). The large discrepancy between theoretical arrival time and observed GW phase for station PMSA might indicate a drastic change in wind and temperature specifications.

S2.10. Infrasound observations at regional networks and arrays

In addition to the IMS and GSN sensors, a number of regional arrays and networks also recorded signals from the Hunga eruption (Fig. S12, Fig. S16 - Fig. S21). These networks provide a dense sampling of the wavefield in regions spread out around the world and allow for in depth

analysis of the temporal and spatial evolution of the signals recorded, as well as a variety of sensors with varying responses (Fig. S1).

S2.11. Seismic

Local ground deformation induced by pressure variations has been observed and modeled in seismic data for decades (e.g., *58,59*). These motions appear as retrograde elliptical in the vertical-radial plane and have amplitudes proportional to the amplitude and propagation speed of the pressure disturbance, inversely related to rigidity of the materials the seismometer is emplaced in, and should be vertically polarized by at least a factor of two (*59*). Ground motions related to the passing of the Lamb pulse were observed on global seismometers (Fig. 2D).

For many stations, the horizontal amplitudes are counter-intuitively larger than the vertical channels. This likely reflects physical tilting of the seismic instrument, which in Earth's gravity field, appears as large horizontal accelerations (*59,60,61*). Consistent with theory, on many borehole seismometers, we observe ground motions which are retrograde elliptical and polarized in roughly the radial direction and with vertical ground velocities phase delayed by 90° from pressure records. We stress that because the Lamb wave propagates much slower than the Rayleigh wave phase velocity of the solid Earth, these ground motions are not reflective of a radiated seismic wave.

S2.12. Ionospheric signature

We identify the signature of the main atmospheric pressure wave followed by tsunami waves both in ionosphere and sea-level data. To do so, we analyze the GNSS observations from the GNSS receiver TUVA near the closest buoy B-I (NOAA/NDBC DART buoy 51425, 1220 km from the volcano). We focus on the GNSS link G-III (see Fig. 4F). Locations of observation points, raw data, and detrended data are shown on Fig. S26 (supporting Fig. 4F). Here, we assume a thin ionospheric shell at 350 km altitude. We highlight two distinct signatures: they have different frequency contents and are distinguished from each other by the theoretical tsunami arrival time at the observation point, computed with the Simple Long Ocean Wave Model (SLOWMO) tool (http://slowmo.sourceforge.net/). In the STEC upper panel, the first signature (also red-shaded in Fig. 4F) is linked to the pressure wave excited by the main explosion and characterized by a very large amplitude (~10 TECU peak-to-peak) and long duration (~1-hour long). The second signature (blue-shaded in Fig. 4F) has the characteristics of short-period internal gravity waves induced by the oceanic tsunami generated directly by the eruption. We isolate this second signature following the classification procedure described by (*62*). The background noise is assessed based on the observations of the day before. As for the sea level panels, we attribute the first signature (red-shaded in Fig. 4F) to the tsunami-like waves forced by the same pressure perturbation following the eruption (similar to the air-sea waves identified by (*8*) after the Krakatau eruption), while the second signature (blue-shaded in Fig. 4F) is the oceanic tsunami. Both the timing and the waveform similarities support the classification of the highlighted signatures.

S2.13. Propagation models for atmospheric infrasound

Acoustic signals are understood as disturbances that propagate through coupled compression and rarefaction, as opposed to buoyancy driven waves that depend on gravity and density gradients. The propagation of acoustic waves can be modeled by solving the equations of

fluid mechanics; however, due to the high computational cost, this is not always achievable, so that severe, yet physically reasonable, approximations are usually made. One common strategy to reduce the computational time is to neglect non-linear terms, which leads to wave-like equations or full-wave models that are valid for small source amplitudes and pressure perturbations (*63*). An additional solution to facilitate propagation modeling is provided by the geometrical acoustics approximation that consists in computing only ray paths without resolving the full wavefield. The geometrical acoustics approximation, or ray theory, is applicable when the scale of spatiotemporal variations in the atmosphere is large compared with the scale of the acoustic wavelengths and periods. It captures the refraction of waves and propagation times but does not model full-wave effects such as diffraction. The geometrical acoustics approximation combines versatility, computational efficiency, and ease of interpretation (*64*). On the other hand, full-wave models capture both refraction and diffraction but can become computationally intensive, in particular when horizontal refraction and interaction with topography are to be included.

In the analysis here, two infrasound propagation models are utilized to provide preliminary simulation results. These include the geometrical acoustics model *InfraGA* (*64*) as well as a full-wave parabolic equation (PE) model *ePape* (*65*). Both models are open-source codes that are available on GitHub. The propagation models rely on atmospheric specifications of temperature, wind and density. The simulations presented in this Supplemental Material are simulated using either the Ground-to-Space (G2S) model or the ECMWF ERA5 (fifth generation ECMWF atmospheric reanalysis) reanalysis model that is provided by the European Centre for Medium-Range Weather Forecast (ECMWF) through the Climate Data Store (*66*). G2S specifications are available through http://g2s.ncpa.olemiss.edu/.

The G2S specifications extend from the ground up to 150 kilometers altitude. This dataset fuses the NOAA-GFS and NASA-MERRA models with the MSIS/HWM climatological models in the mesosphere and thermosphere using a spectral method (*67*). The ERA5-HRES model extends from the ground up to 80 km altitude, is available with hourly temporal resolution and has a spatial resolution of $0.25° \times 0.25°$. Beyond 80 km altitude, ECMWF models are combined with NRLMSIS00 atmospheric (*68*) and HWM14 wind (*69*) models using a spline interpolation between 75 and 85 km altitude.

S2.14. Global ray tracing

The propagation of infrasonic waves from the Hunga eruption has been investigated using the spherical geometry methods in the *infraGA* infrasonic ray tracing software (*64*). Atmospheric specifications have been pulled from G2S for a 60 x 60 latitude-longitude grid over the globe, which results in 3° and 6° resolution in latitude and longitude, respectively. The grid accounts for the finite infrasonic propagation speed by delaying the reference time at locations farther from the source using an estimated infrasonic celerity of 290 m/s (e.g., a grid node 5,000 km from the source uses a reference time approximately 5 hours after the estimated origin time). This temporal delay in the grid is valid for the direct propagation of infrasound but cannot be applied for paths beyond the antipode.

A preliminary global scale simulation is shown in Fig. S28 for a fixed inclination angle of 15° where propagation paths have been computed for the first 20 hours allowing the energy to propagate from the source to near the antipode. Ray paths are found to deviate from great circle paths due to crosswind effects as well as latitudinal and longitudinal variations in the atmospheric structure; though, relatively large zonal wind variations with latitude are likely dominating these effects. Propagation paths converge at various locations as waves approach the antipode but don't

focus at the antipode as one might expect for great circle paths from the source to the antipode. These deviations are likely explanations for observed direction-of-arrival differences from the known source location at various arrays. The arrival locations where propagation paths intercept the ground surface for paths covering multiple inclination angles from a more robust simulation is included in Movie S 7, which includes a number of interesting features including fast moving, stratospheric arrivals to the west of the source as well as a separation of antipode foci locations due to the crosswinds and latitudinal and longitudinal sound speed and wind gradients discussed above.

S2.15. Global PE results towards IMS stations

Ray tracing is a high-frequency approximation which neglects diffraction effects. Such approximation becomes less accurate when fine-scale structures in the atmosphere are comparable to the acoustic wavelength. This leads to the emergence of acoustic shadow zones where the acoustic energy is predicted to be zero at the ground which is not physical. To account for lower-frequency effects, we simulate the infrasound ground amplitudes from the Hunga eruption using the ePape Parabolic Equations software (PE, see Supplementary Text S2.13) together with ECMWF ERA5 atmospheric models over the entire globe at 10:00 UTC on 15 January 2022. We compare PE simulations to observed acoustic amplitudes at each IMS station by integrating infrasound amplitudes, from the first arrival (A1), in the frequency domain between 0.47 and 0.053 Hz.

Predicted attenuations for 15 January are the lowest in the regions of strong stratospheric winds blowing along the direction of propagation east of North America and west of Hunga volcano (Fig. S27A), which is in good agreement with observations at IMS stations south and southwest of the volcano (Fig. S27C). This is also in line with models of global infrasound propagation showing that infrasound paths are primarily controlled by strong stratospheric winds over 25 km altitude (67). Yet, PE predictions greatly overpredict infrasound amplitudes at most stations northwest and east of Hunga volcano. In particular, PE simulations for stations east of Hunga volcano, such as IS13, predict extremely large attenuations (< -150 db), despite clear infrasound observations at these locations. This highlights the limitation of PE simulations to capture the full acoustic wavefield (PE neglects Earth ellipticity and relies on an effective-velocity approximation) and possibly the accuracy of available atmospheric wind models above the stratosphere.

S2.16. Back azimuth deviations

We observe a back azimuth shifting with time over a few hours corresponding to the refracted infrasound phases coming after the first Lamb wave. The effect is noticeable at many of the infrasound arrays in Europe, over a wide range of latitudes. It could be attributed to crosswinds distorting the path of infrasound traveling along other great circles.

The array processing results at IMS infrasound array IS37 at Bardufoss, Norway illustrates the effect (Fig. S22, left panel). There is a uniform shift in back azimuth (from higher to lower values) for the infrasound arrivals that arrive between 18:00 and 20:30. The trend is followed by another set of detections that show a trend in the opposite direction. This effect is seen at many of the other stations. For the US-based IMS stations on the West Coast, the shift in back azimuth is more noticeable for the antipodal arrival which crosses the circumpolar vortex.

An initial interpretation follows from the analysis of ECMWF ERA5 model data. Fig. S22 (right) shows the adiabatic sound speed, along-track, cross-track wind and effective sound speed as a function of range and altitude for the path from Hunga volcano to IS37. The jetstream and circumpolar vortex are clearly visible as crosswinds around the range of 6000 km. The eastward circumpolar vortex leads to the detection of infrasound that originally had a more westward propagation azimuth (e.g. *70*).

Predicted arrival characteristics at I37NO using spherical geometry ray tracing results extracted from data used in Movie S 7 shows a spread of arrival celerities between 242 and 256 m/s with back azimuths from -21° to -33° and a trend moving more negative later in the wavetrain. While this trend appears similar, there are notable differences between these predicted arrivals and the observations summarized in Fig. S27, demonstrating the need for more robust propagation modeling capabilities as well as improved atmospheric specifications.

The effective sound speed ratio can be used to obtain qualitative insight into how infrasound is ducted. In this case, values larger than one mean that ground-to-ground propagation is efficient. In the plots, the thermospheric waveguide (which is always there, but is also more absorptive) is not included because the ECMWF model top is at 80 km. The effective sound speed ratio indicates that infrasound could be efficiently ducted between the ground and ~20-40 km altitude between ~9,000 and 14,000 km range from Hunga volcano. This is related to the occurrence of a minor Sudden Stratospheric Warming (SSW) that developed over Russia in the beginning of January 2022. Indeed, an increase in adiabatic sound speed (related to temperature) can be noted over the North Pole. Minor SSWs occur frequently in the boreal winter hemisphere and are known to have a profound effect on infrasound propagation conditions (*71*).

S2.17. Pressure record in the deep ocean

The Lamb waves were also recorded as a pressure pulse in the deep ocean. Deep ocean tsunamimeters (Fig. S29A,B) in the Pacific operated by the National Oceanic and Atmospheric Administration (NOAA) were triggered by the arrival of pressure waves (Fig. S29B). We picked the peak arrival time because the first arrival of a slowly increasing signal is difficult to pick. The propagation speed of the leading impulsive pressure peak is 298 m/s, which coincides with the Lamb wave pulse propagation speed. The propagation speeds vary a little among stations.

A peculiar feature of the pressure pulse observed in the deep ocean is that the amplitude is about two (or more) times larger than the subaerial pressure pulse. The peak amplitudes on a few stations out of 10 in Fig. S29A exceed 6 hPa, with an average of more than 4 hPa. On land outside Tonga, the maximum observed peak amplitude does not exceed 6 hPa except the station at 756 km from Tonga. If the pressure propagation speed is much less than the tsunami propagation speed, we expect that the pressure perturbation at the sea surface is not recorded at the deep ocean. The dynamic process of the fast-spreading pressure pulse along the ocean surface likely caused this excess pressure impulse in the deep ocean bottom. The deep ocean tsunami records are especially useful for filling the large observational coverage gap in the ocean. To utilize the tsunami records, we need to understand the mechanism of the pressure increase and establish a method to retrieve a subaerial pressure.

S2.18. Tsunami generation by the leading pressure pulse

Coastal communities reported Tsunamis generated by the Hunga eruption. An investigation of tide gauge records, nearby barograms and deep ocean tsunamimeters in, and close to, Japan

(Fig. S30A) indicates that the leading pressure pulse observed in the deep ocean (Fig. S30B) does not cause the primary damage to coasts.

The ocean bottom pressure signal (Fig. S30A, top two records) starts with an impulsive pressure, as found in the Pacific in Fig. S29, and the shape of this pressure pulse is similar to subaerial barograms (Fig. S30A, bottom two records) except that the deepwater pressure amplitude is two times larger or more (confirming the pressure amplification at the deep ocean by direct observation). As the Lamb wave pulse goes over the coastal tide gauge, it does not immediately respond to the pressure peak. After the pressure peak passes, the tide level slowly and gradually grows. The tide-level oscillations increase in amplitude for up to 2 to 6 hours after the passage of the pressure pulse (Fig. S29B), consistent with the reports from JMA.
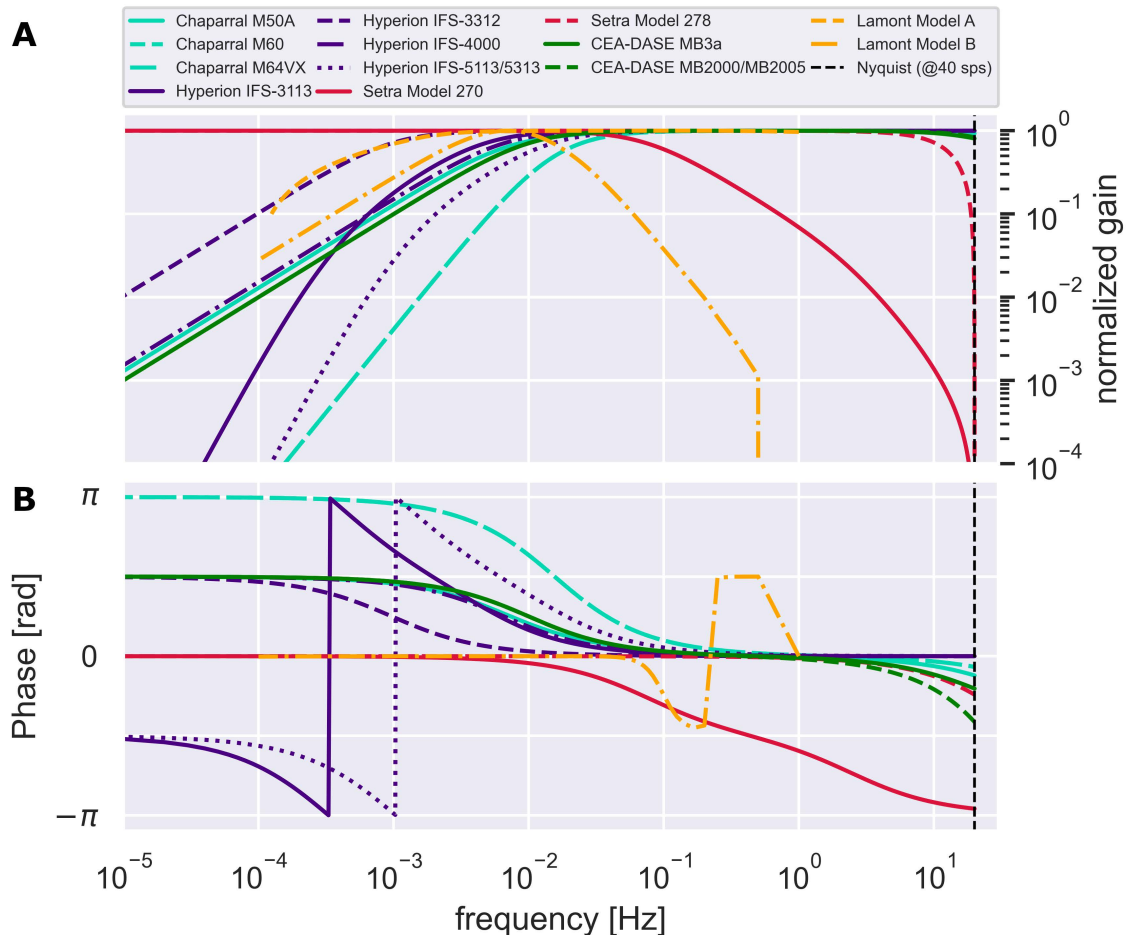
Fig. S1. Frequency response of barometers and microbarometers used in this study.
(**A**) Amplitude and (**B**) Phase between 0.01 mHz – 50 Hz. Sensors are grouped by color according to manufacturer. For comparison, response curves of the Lamont microvariobarograph sensors (*16,72,73*) have been included (orange dashed lines).
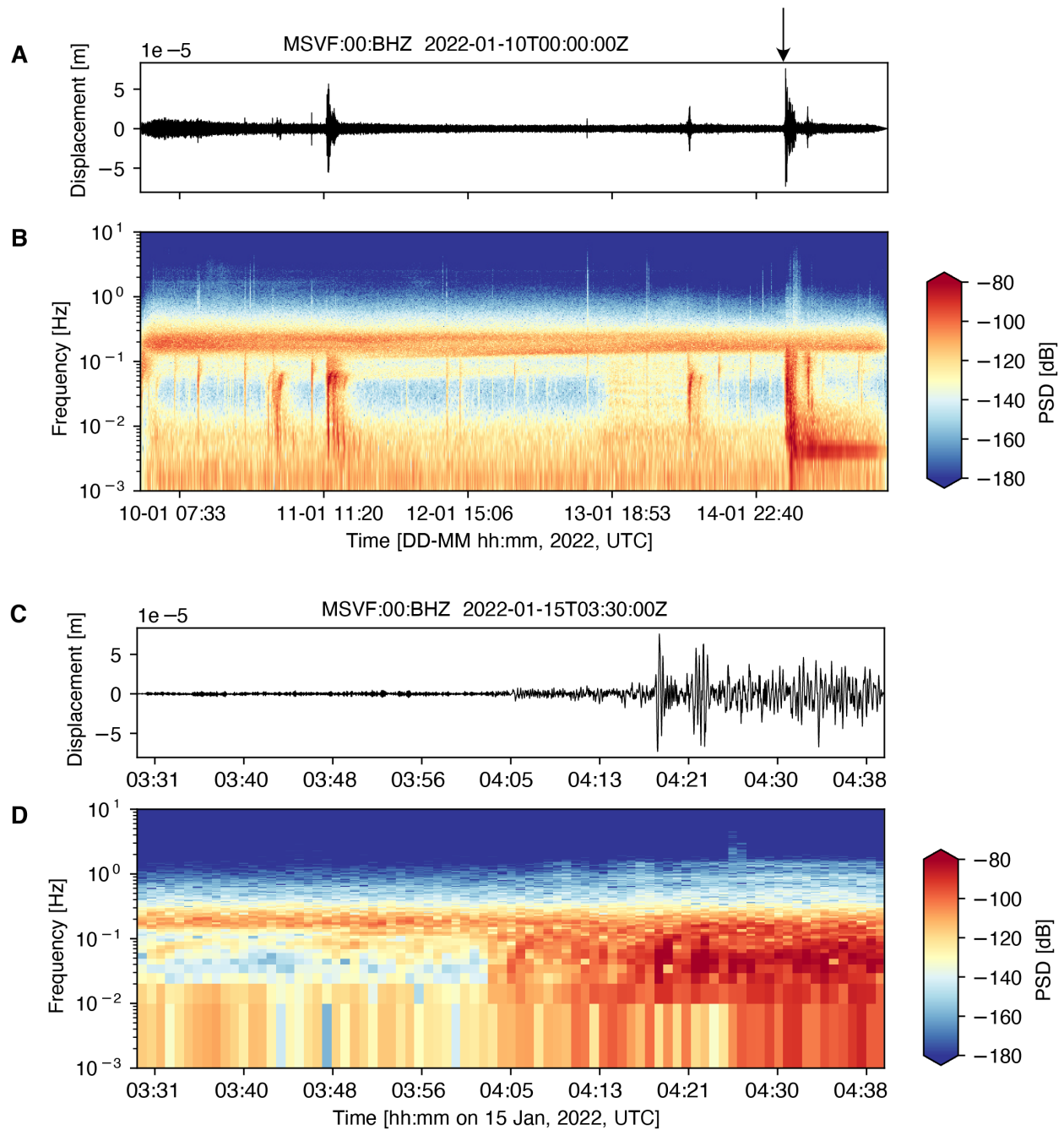
Fig. S2. Seismic data for station MSVF, Fiji.
Seismic analysis at station MSVF for (**A**, **B**) multi-day time series and (**C**, **D**) ~ 1 hour long time series showing the eruption onset. (A, C) Displacement waveforms with the instrument response corrected using ObsPy (*29*). (B, D) Power spectral density spectrogram of ground displacement, with dB reference for the spectrogram of 1 m²/Hz. Spectrogram windows are (B) 10000 sec and (D) 100 seconds, with an overlap of 50% for both. Spectrograms were created using the built-in spectrogram function in Matplotlib with PSD mode. The colors correspond to spectral amplitudes (i.e., blue and red to low and large amplitudes, respectively).
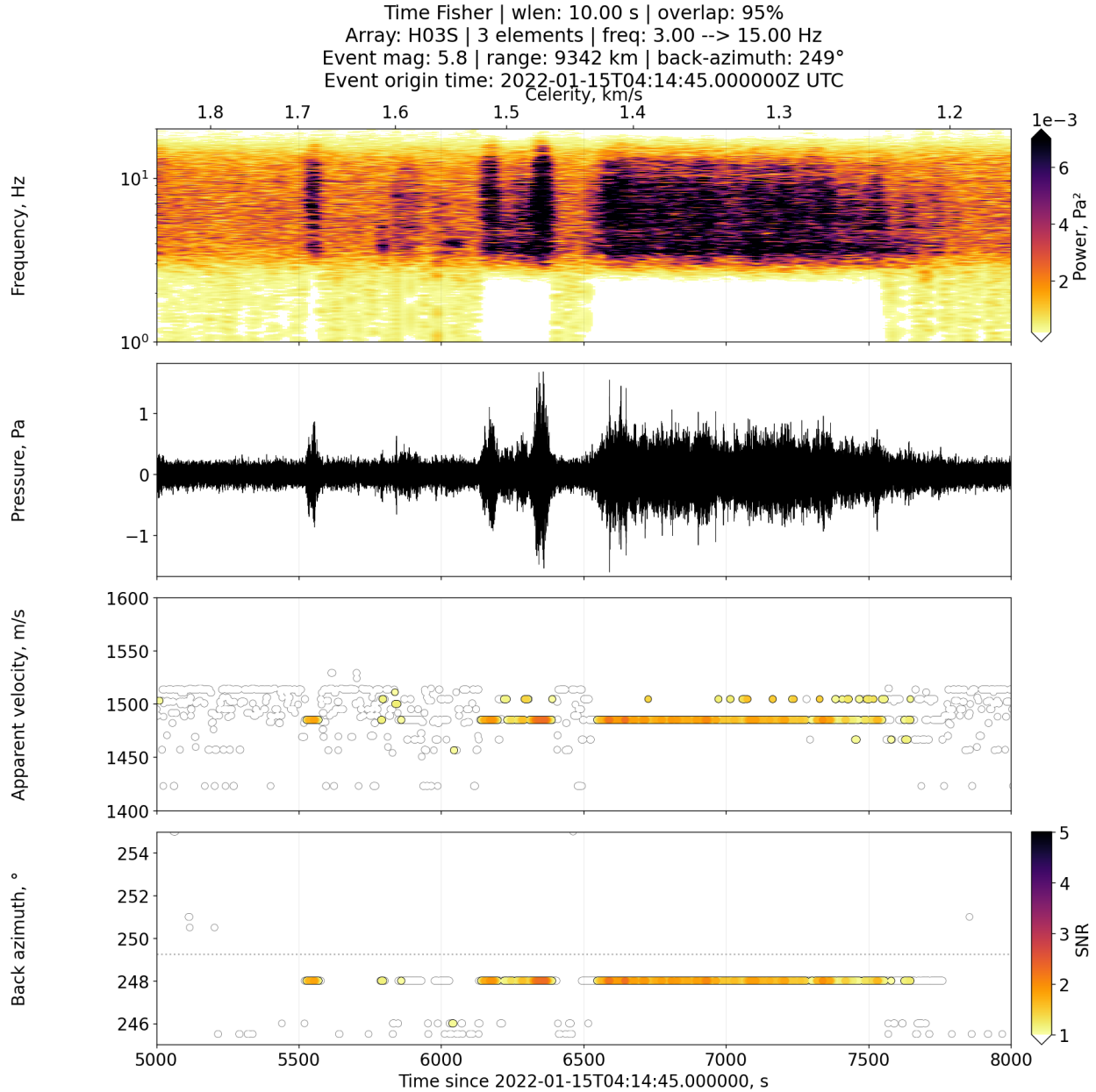
Fig. S3. Array processing results from IMS hydroacoustic station HA03 (H03S, south triplet).

Data were resampled from 250 to 100 Hz, bandpass filtered between 3 to 15 Hz, and a 10-second sliding window with 95% overlap was used. The slowness grid was set to have an azimuthal resolution of 0.5 degrees and an apparent velocity resolution of 0.5 m/s. We use the algorithm by (*46,74*), which is a delay-and-sum time-domain beamformer combined with the Fisher statistics.
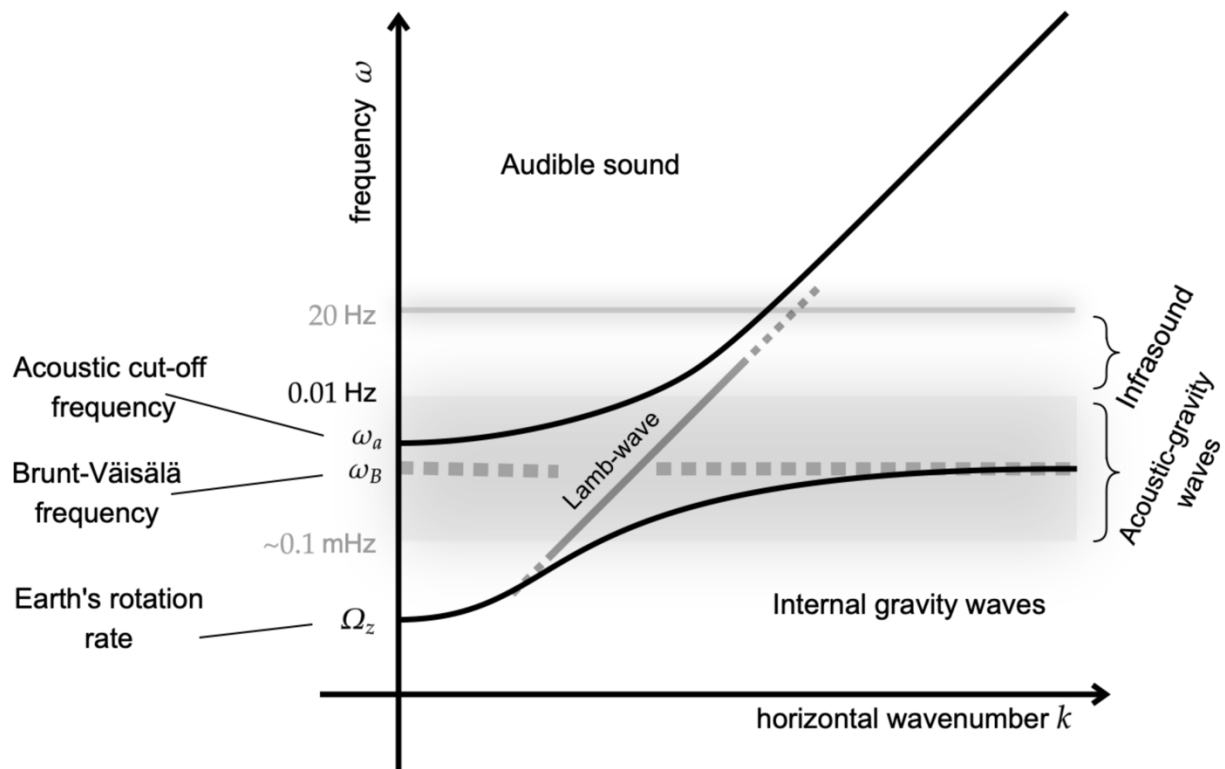
Fig. S4. Schematic overview of wave dispersion.
Schematic overview of the dispersion of acoustic waves, acoustic-gravity, and gravity waves as a function of frequency and horizontal wavenumber. The group speed is defined as the ratio of frequency and horizontal wavenumber. The Lamb wave appears as an acoustic-gravity wave with a group velocity of ~315 m/s. Figure adapted from (*4*).
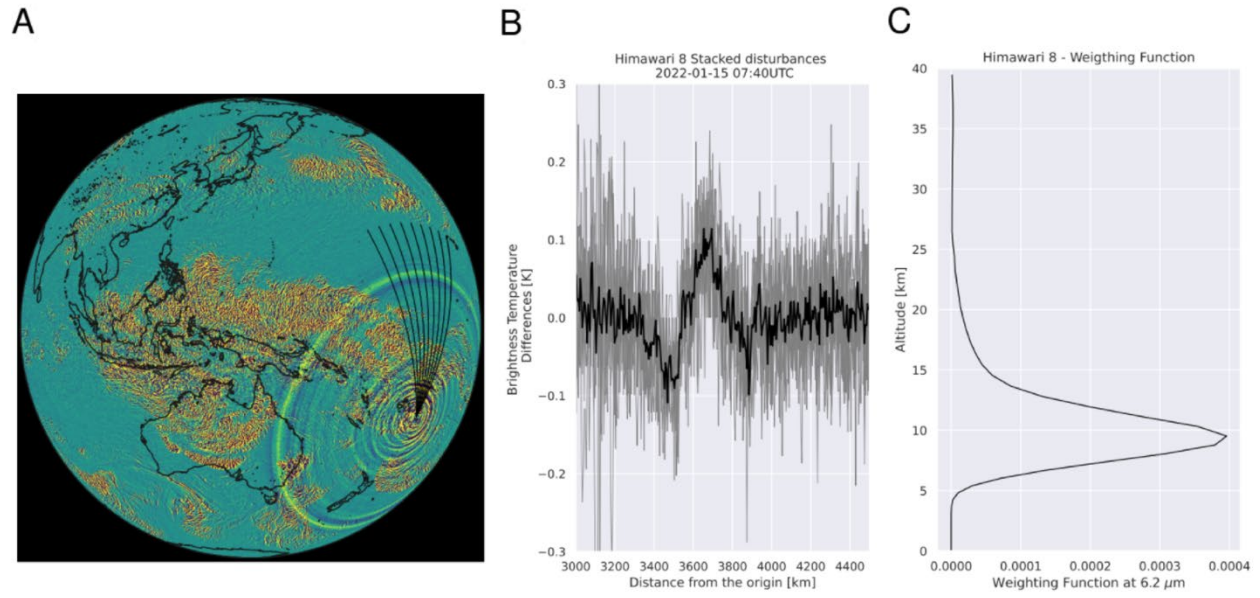
Fig. S5. Tropospheric signature of the Lamb wave.
(**A**) Azimuth selection (340°, 345°, 350°, 355°, 360°, 5°, 10°, 15°, and 20° from the source location) overlaid on the Himawari8 snapshot taken at 07:40 UTC on 15 January 2022. (**B**) Himawari8 radial stack of brightness temperature differences at 07:40 UTC for the selected azimuths, highlighting the tropospheric Lamb wave signature. (**C**) Weighting function at 6.2 μm, indicating the altitudes contributing the majority of the measured radiation.
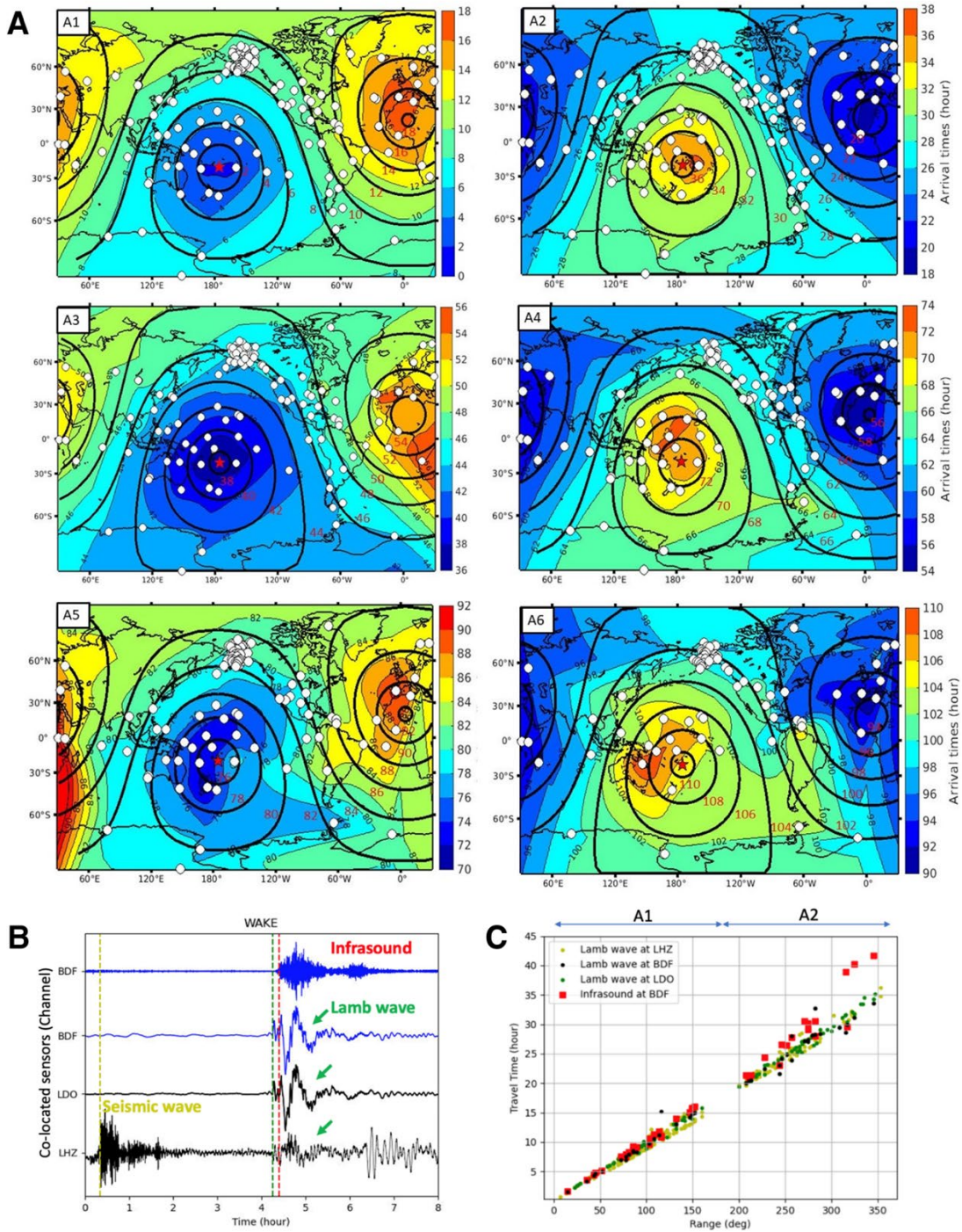
Fig. S6. Contour map of Lamb wave arrival times from the Hunga eruption for 6 passages (A1-A6) and co-located infrasound, barometer, and seismometer at WAKE.
(**A**) Contours were estimated from GSN, IMS, and AK stations (white circles) and compared with arrivals assuming a fixed 0.3 km/s group velocity (black contour). (**B**) The example plot shows seismic, infrasound and Lamb waves recorded at co-located infrasound sensor (BDF), barometer (LDO), and seismometer (LHZ) of WAKE (one of the GSN stations). (**C**) Comparison of traveltimes of infrasound and Lamb waves for the first (A1) and second (A2) arrivals.
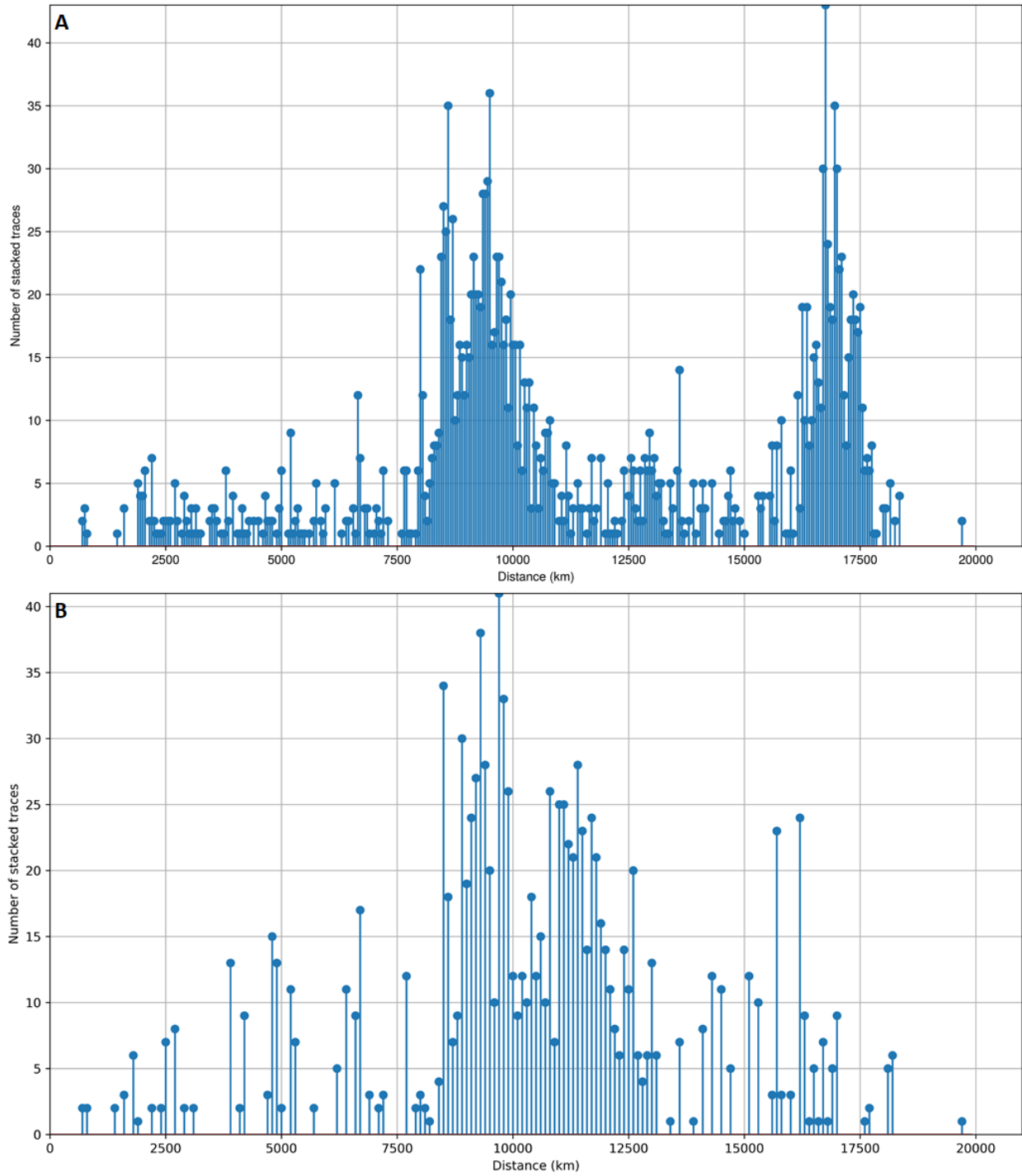
Fig. S7. Number of aggregated traces per distance bin.
(**A**) Number of seismic traces aggregated by 50 km distance bins in Fig. 2D. (**B**) Number of pressure sensor/barometric traces aggregated by 100 km distance bins in Fig. 2B,C.
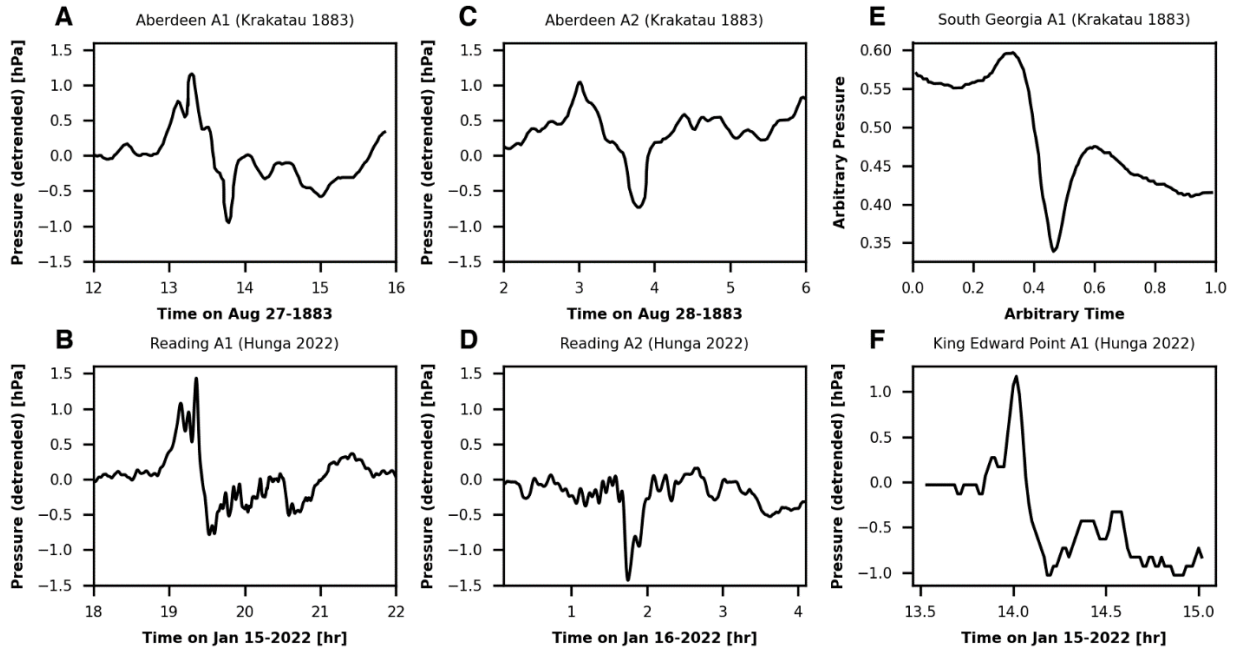
Fig. S8. Waveform comparison for Hunga 2022 and Krakatau 1883 at select stations.
(**A, C**) Digitized and calibrated waveforms for the A1 and A2 arrivals of the Krakatau 1883 eruption at Aberdeen, respectively (*12*). (**B, D**) A1 and A2 arrivals of the Hunga 2022 eruption in Reading (lowpass below 5 minutes), respectively. (**E**) Digitized and uncalibrated waveform for the A1 arrival of the Krakatau 1883 eruption at South Georgia (*12*). (**F**) A1 arrival of the Hunga 2022 eruption at King Edward Point (South Georgia).
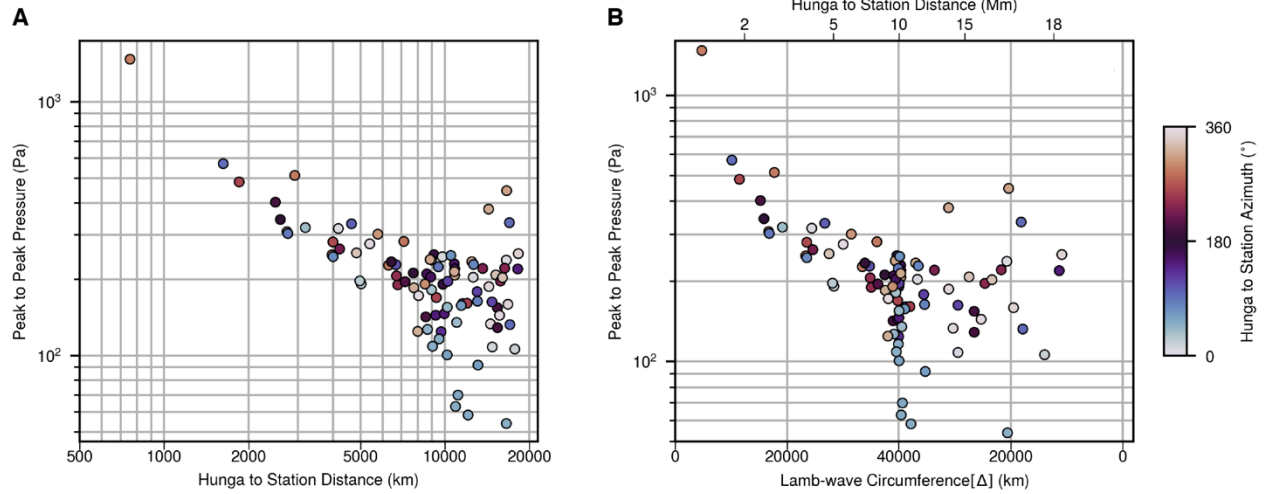
Fig. S9. Reduction of Lamb wave amplitude.
The reduction in Lamb wave peak-to-peak amplitude in the $[1\times10^{-4}, 1\times10^{-3}]$ Hz passband as a function of (**A**) distance from Hunga volcano and (**B**) the circumference of an undistorted circular Lamb wave at the distance of each station (Lamb wave Circumference [Δ]).
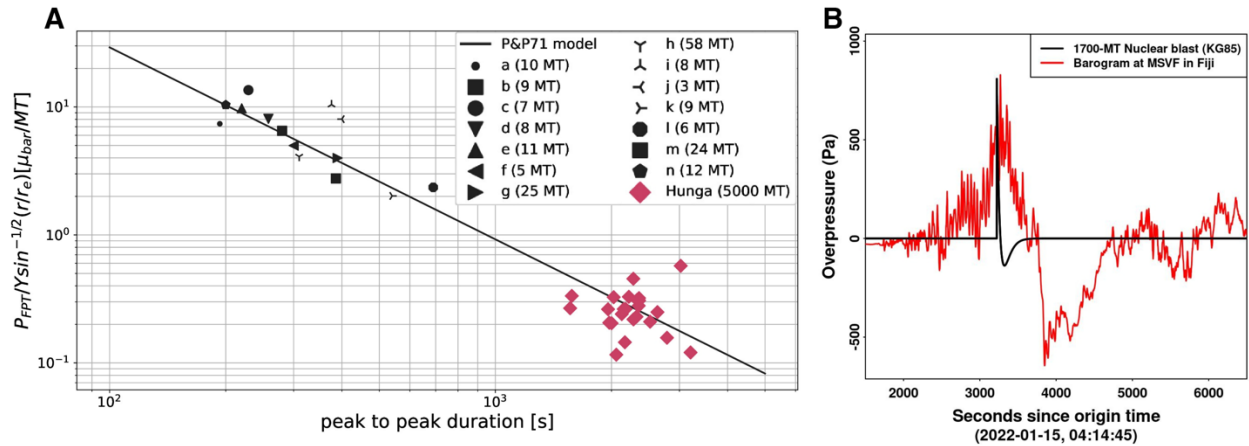
Fig. S10. Attempted yield estimates and barogram comparison with theoretical nuclear blast waveform.
(**A**) Nuclear detonations (black symbols) and Hunga eruption data (red symbols) plotted alongside the proposed model (black line). Hunga eruption data are scaled by the average estimated yield (see legend) across all stations rather than by each station's estimated yield. Reported yields from nuclear detonations (*14*) are given in the legend. (**B**) Barogram recorded at station MSVF in Fiji (756 km) compared with a theoretical nuclear blast waveform predicted for a 1700-MT nuclear explosion at the same distance.
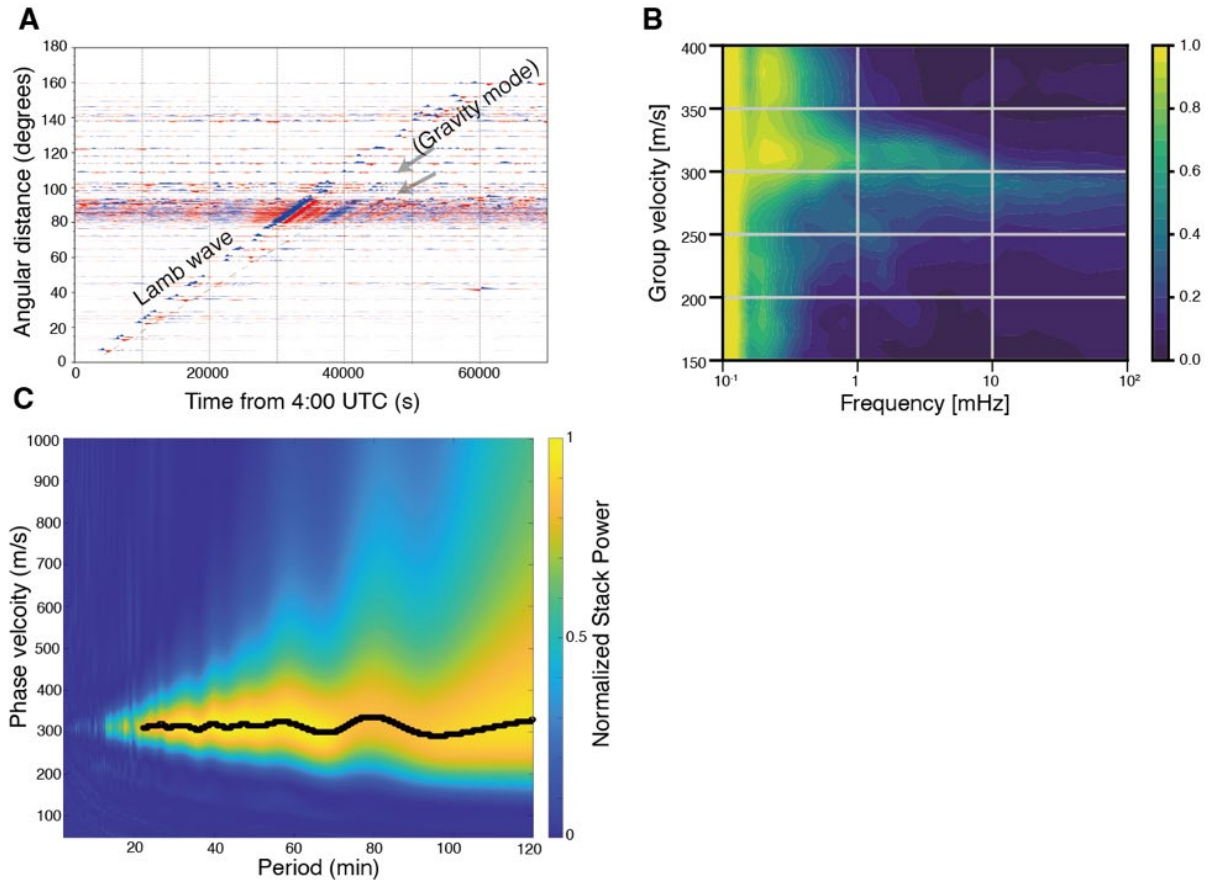
Fig. S11. Dispersion of atmospheric waves.
(**A**) Barometric (0.1-2 mHz) records of LDO channels at stations of networks AK, II, and IU against angular distances from Hunga volcano. This figure shows clear Lamb wave propagation, and the dashed line and the arrows show the later phases. The group velocity of the faster phase recorded is about 260 m/s with the dispersion, which may be explained by an atmospheric gravity mode (*8*). A slower phase is shown by the rightmost arrow, although this observation is more ambiguous. These later phases depend on the local conditions and are therefore less clear than the Lamb wave phases. (**B**) Frequency-Time Analysis (FTAN) of atmospheric pressure data. We calculated FTAN diagrams (*75*) of LDO channels at IU stations and stacked them. (B) incorporates data starting 30 minutes before the origin time of the Lamb wave in (A). Above 3 mHz, the group velocity decreases with frequency. The observed dispersion suggests that fundamental acoustic modes could be dominant above 5 mHz (*48*). The diagram also shows a wave packet at around 1 mHz with a group velocity of about 250 m/s, which could be explained by a fundamental gravity mode (*8*). (**C**) Dispersion diagram of the Lamb wave using 71 of the AK LDO stations with a time window from 11:00-17:00 UTC. It assumes great circle path propagation between Hunga volcano and the stations. The F-K analysis is performed in terms of phase velocity and period of the Lamb pulse between 2-120 min period. This diagram shows a less dispersive feature with phase velocity around 310-320 m/s.
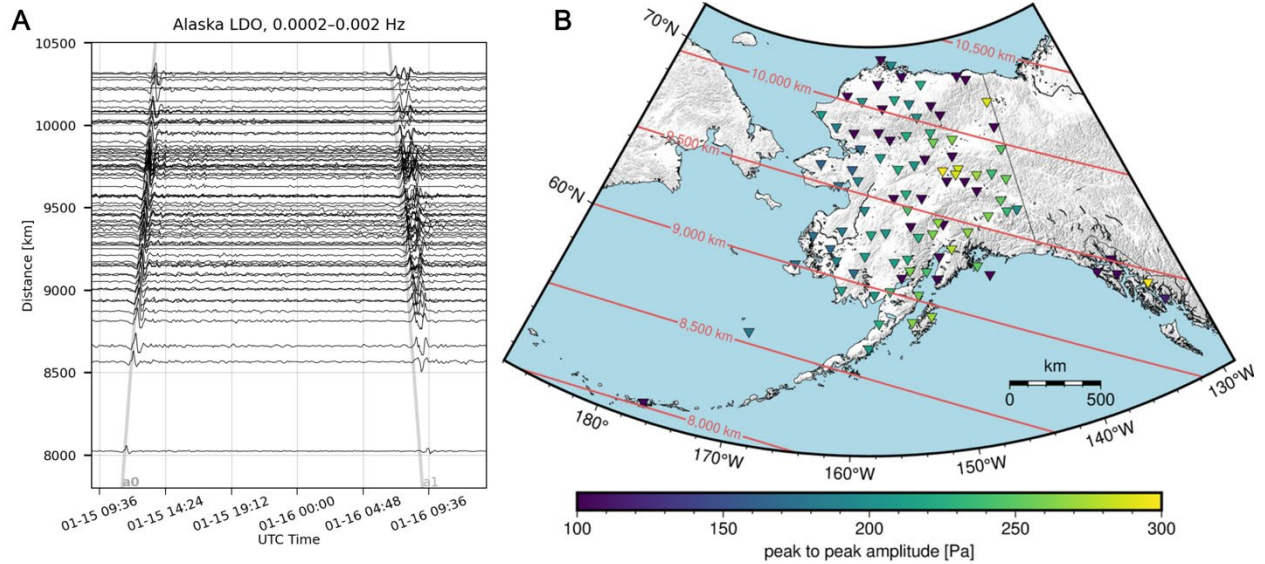
Fig. S12. Alaska barometric pressure data.
(**A**) Record section of detrended and filtered (5000–500 s) data between 2022-1-15 09:00 – 2022-1-16 14:00 UTC. All stations with LDO channels are sorted by range to Hunga volcano. The A1 and A2 arrivals are clearly seen across all stations; gray lines indicate a 0.31 km/s moveout for each arrival. The A2 (antipodal) arrival shows a 90° phase shift. (**B**) Map of peak-to-peak pressure amplitudes across Alaska. Red lines are distance contours to Hunga volcano. Amplitudes vary considerably across the region, ranging from ~100–300 Pa. Amplitudes are determined using the same method as shown in Fig. 2F and described in the Supplementary Text section S2.8.
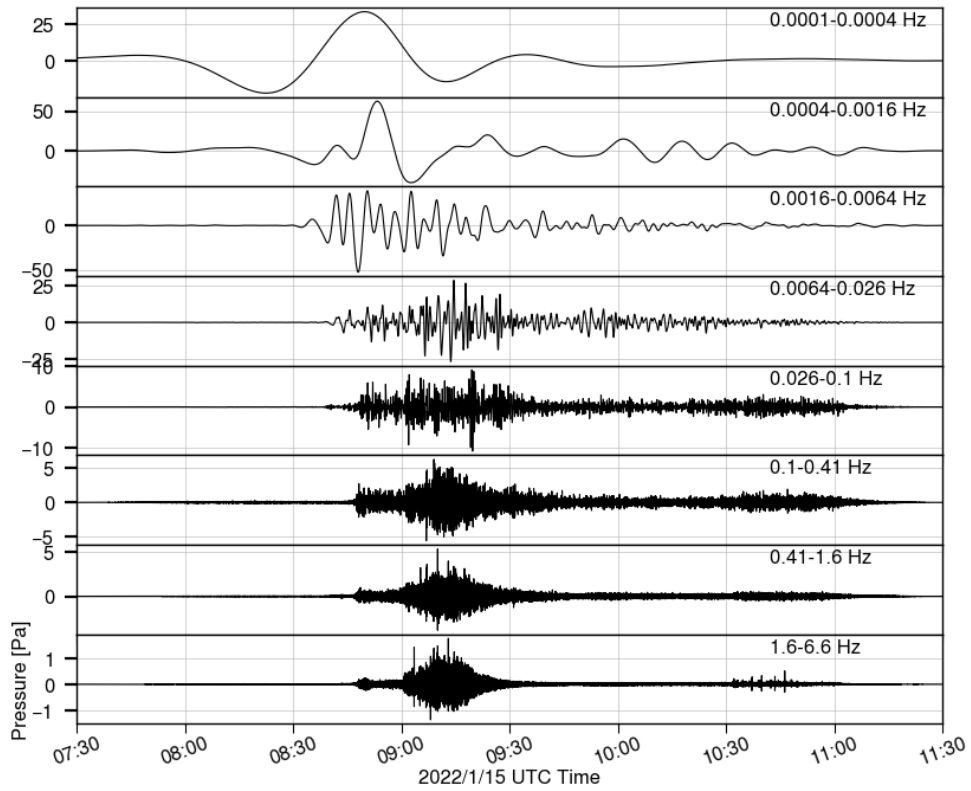
Fig. S13. Infrasound dispersion.
Infrasound data filtered in consecutive 2-octave bands between 10,000 s and 6.6 Hz for station IS59. Clear dispersion is present, as the very low frequency Lamb wave arrives first, followed by increasingly higher frequency energy.
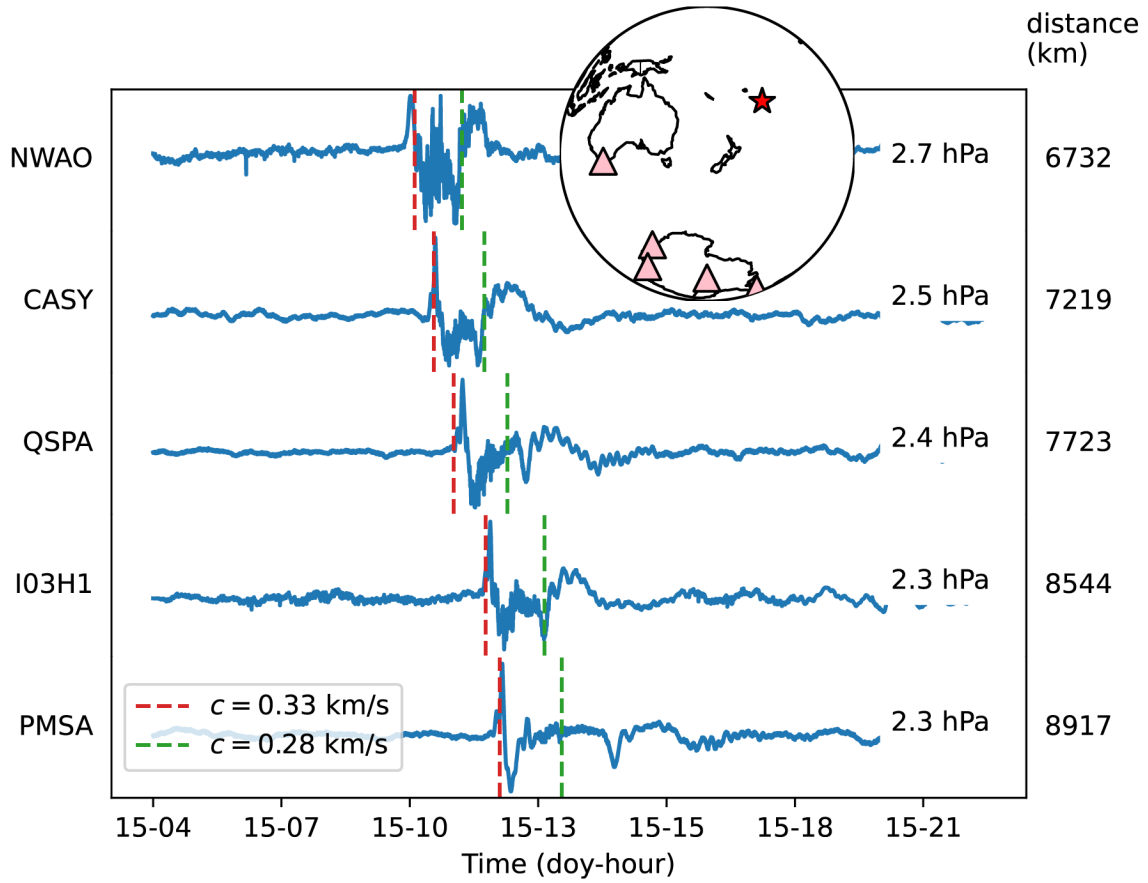
Fig. S14. Gravity wave arrivals.
Barometer and microbarometer waveforms recorded west and southwest of Hunga volcano showing a GW arrival. Vertical lines show theoretical arrival times for a wave traveling at 0.33 km/s (red) and 0.28 km/s (green).
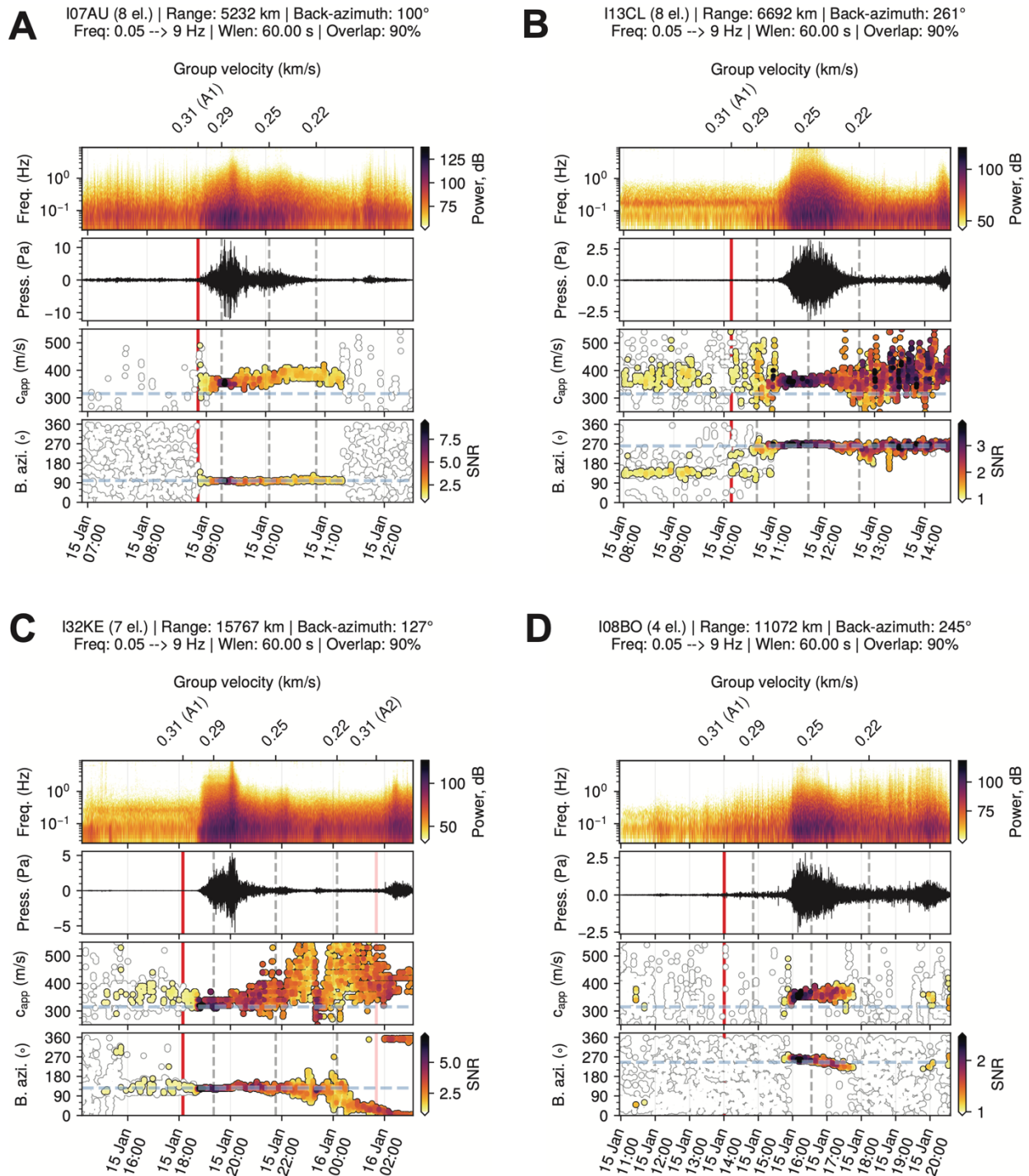
Fig. S15. IMS infrasound array processing.
(**A, C**) Infrasound group velocities line up to approximately 290 m/s for stations towards the west of Hunga volcano. (**B, D**) Towards the east of Hunga volcano, infrasound group velocities line up around 250 m/s. This is in line with typical group speeds for stratospheric and thermospheric waveguides.
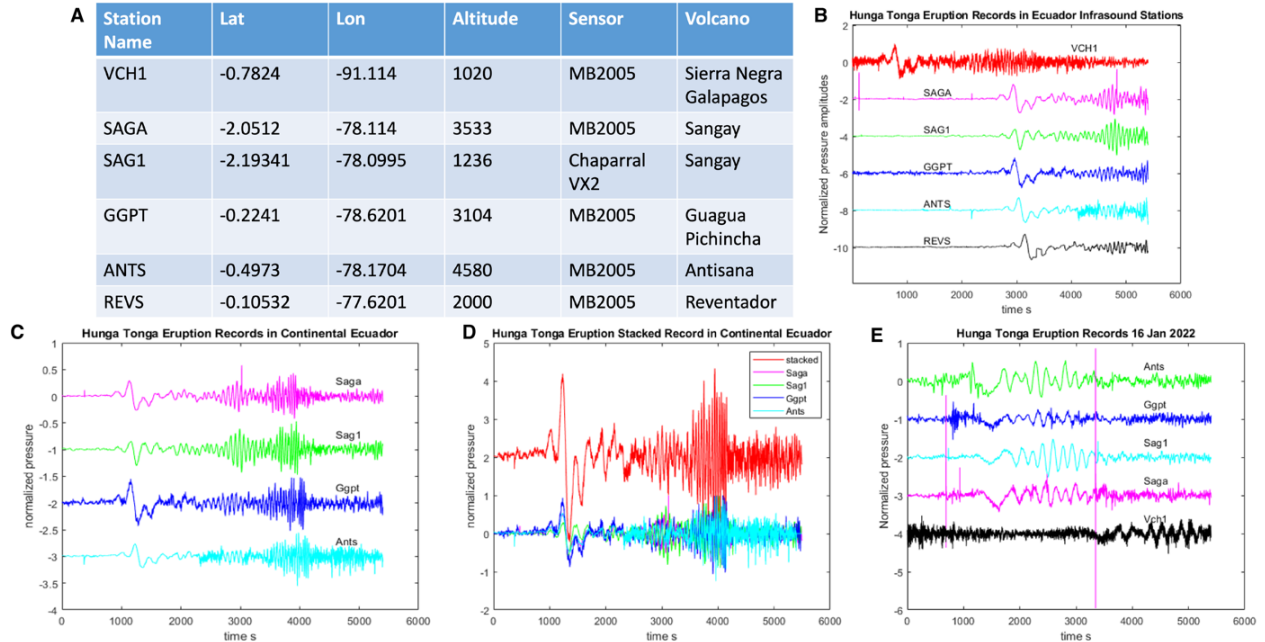
Station Name	Lat	Lon	Altitude	Sensor	Volcano
VCH1	-0.7824	-91.114	1020	MB2005	Sierra Negra Galapagos
SAGA	-2.0512	-78.114	3533	MB2005	Sangay
SAG1	-2.19341	-78.0995	1236	Chaparral VX2	Sangay
GGPT	-0.2241	-78.6201	3104	MB2005	Guagua Pichincha
ANTS	-0.4973	-78.1704	4580	MB2005	Antisana
REVS	-0.10532	-77.6201	2000	MB2005	Reventador

Fig. S16. Regional data processing from Ecuador.
(**A**) Station's location and sensor. (**B**) Low frequency signal recorded at VCH1 (Galápagos) on 15 January 2022 at 12:39:44 (UTC). Largest pressure perturbation with 470 s period. On 15 January 2022 at 13:32 (UTC) pressure tremor with a dispersive wave train beginning with a 128 s period. Blank portions of REVS were filled with an average of a 500 s pre-blank window. (**C, D**) Stacked signal after correction of delay times of the largest pulse arrival times (red on right hand plot). It shows low frequency (gravity waves followed by acoustic tremor with a dispersive pattern. (**E**) Second signal recorded at VCH1 station on 16 January 2022 at 07:40:18 (UTC). Note earlier arrivals at stations in the continent. Peaks (spikes) at SAGA and later at SAG1 are Sangay volcanic explosions.
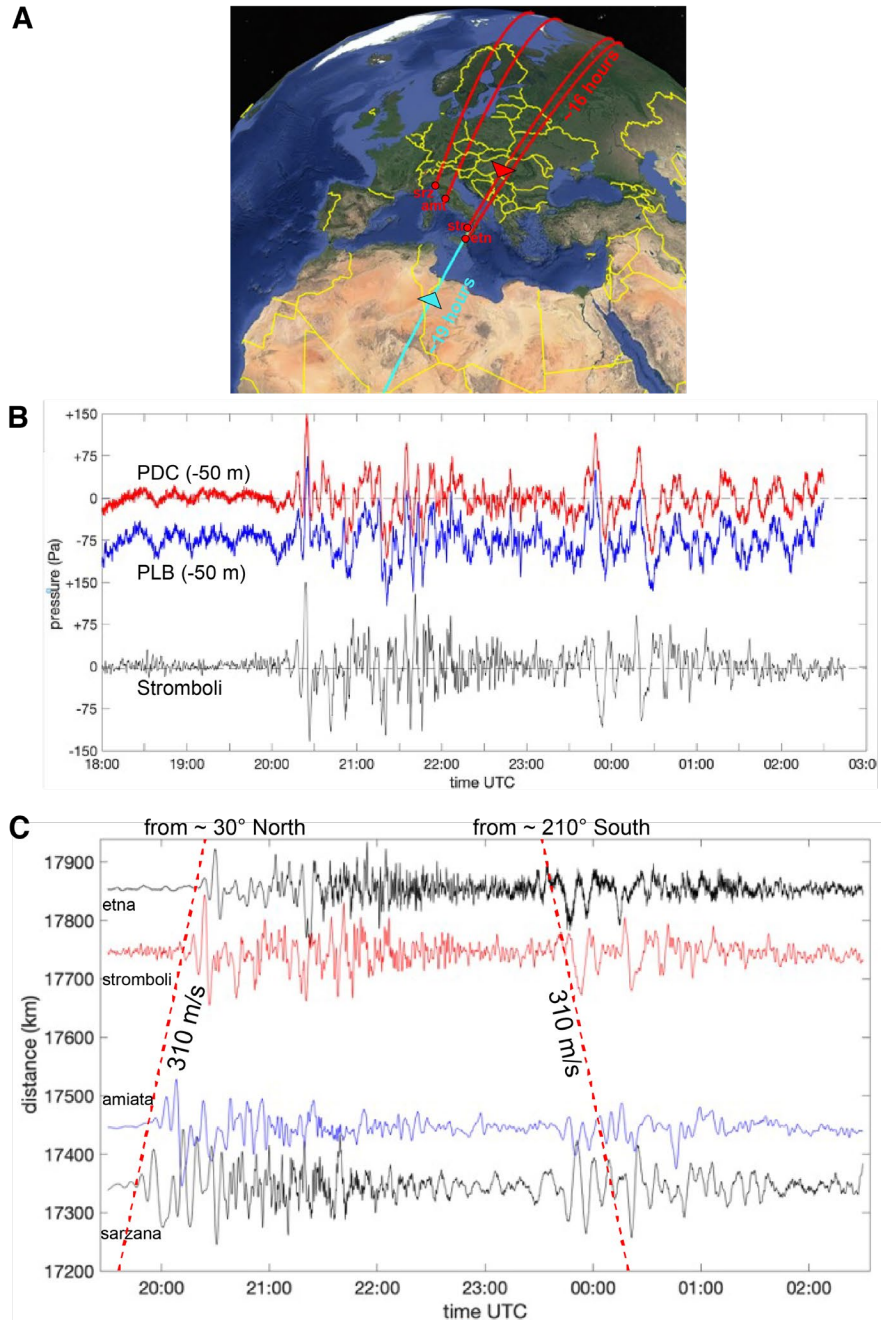
Fig. S17. Regional data processing from Italy.
(**A**) Map showing the position of four pressure sensors in Italy detecting the direct (red) and the antipodal (cyan) arrivals from the Hunga eruption. (**B**) Sample of pressure data recorded at Stromboli Volcano in southern Italy. Blue and red lines are absolute pressure recorded underwater at a depth of 50 m by Tsunami pressure gauges located 300 m offshore. The amplitude of 150 Pa recorded underwater coincides with the amplitude recorded on land Stromboli (black line), and it is roughly equivalent to a sea level change of 1.5 m. (**C**) Pressure signals recorded by four sensors in Italy (A) showing the direct and antipodal Lamb wave arrivals, both propagating at 310 m/s. The black signal recorded in Sarzana was kindly provided by Lunitek.
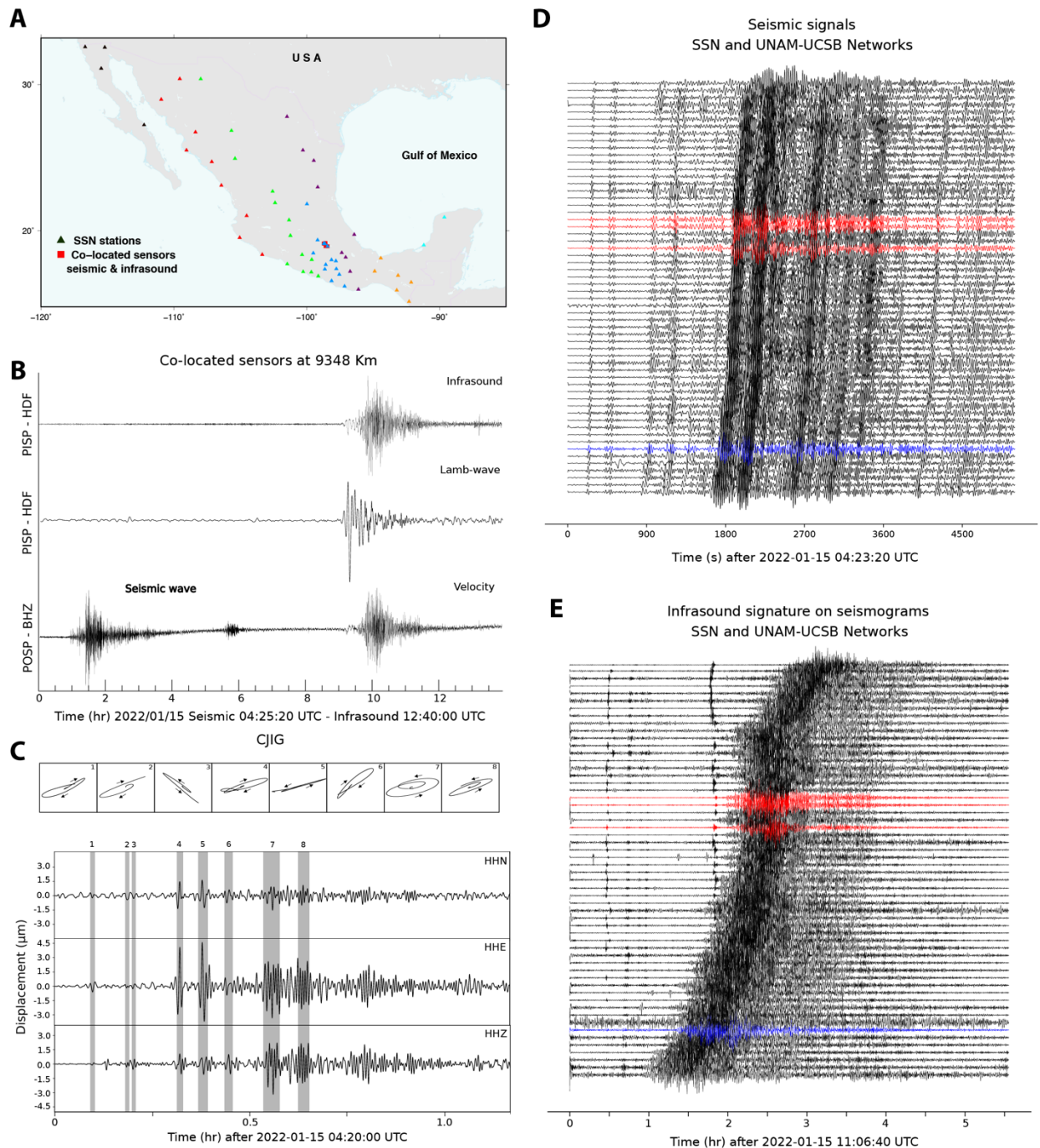
Fig. S18. Regional data processing from Mexico.
(**A**) Recorded Hunga eruption signals across Mexico at 54 Servicio Sismológico Nacional (SSN) broadband seismic stations (120 s), and at 4 stations with co-located seismic (120 s) and infrasound sensors (one 0.01-100 Hz and three 0.03-200 Hz). Triangles indicate local first arrival times at ten second intervals. Source-station distances vary from 8,600 to 10,400 km. (**B**) Records from co-located stations; wavetrain oscillations are visible after low-pass filtering (<0.02 Hz). Panels indicate: (top) Infrasound raw trace, (middle) Lamb wave after bandpass filtered (0.001-0.01 Hz), and (bottom) seismic trace. Station name and component of each normalized trace are indicated

on the y-axes. (**C**) Particle motion trajectories in the horizontal plane for each seismic wave package (shaded), obtained in the 0.01-0.05 Hz band (top panels), indicate strong *Rg* waves that propagate at a local average speed of 3.64 km/s (D). Arrows indicate direction of motion. (**D**) Vertical velocity records, bandpass filtered (0.01 - 0.05 Hz) and downsampled to 1 Hz, exhibit first *P* arrivals approximately eleven minutes after the eruption. SSN traces in black, UNAM-UCSB network in red and the seismic trace used in (C) in blue. (**E**) In the same records, the infrasound signature appeared ~08:11 hours. after the eruption onset. All traces shown have the instrument response removed.
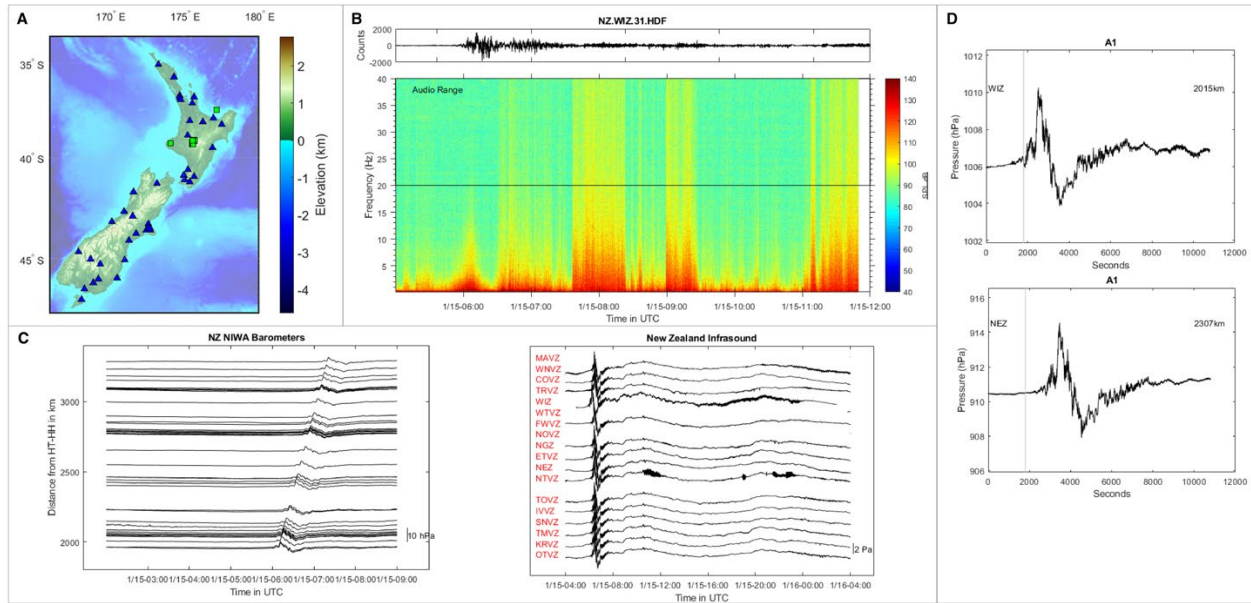
Fig. S19. Regional data processing from New Zealand.
(**A**) Map showing stations used throughout New Zealand. Infrasound (pressure transducers and microbarometers) are plotted as green circles, while barometers provided by National Institute of Water and Atmospheric Research (NIWA) are plotted as blue triangles. (**B**) Waveform and spectrogram of the infraBSU sensor at station WIZ. Reports of audible sounds from the eruption were received throughout New Zealand, and spectral analysis presented indicates that the audio component occurs after the Lamb wave and towards the end of the infrasonic signal, similar to Alaska. (**C**) Waveforms from the NIWA barometer network processed into 1-minute waveforms on the left, and the Setra 270 pressure transducer network on the right. (**D**) Details of the first arrival A1 at the closest (WIZ at 2,015 km) and farthest (NEZ at 2,307 km) Setra sensors.
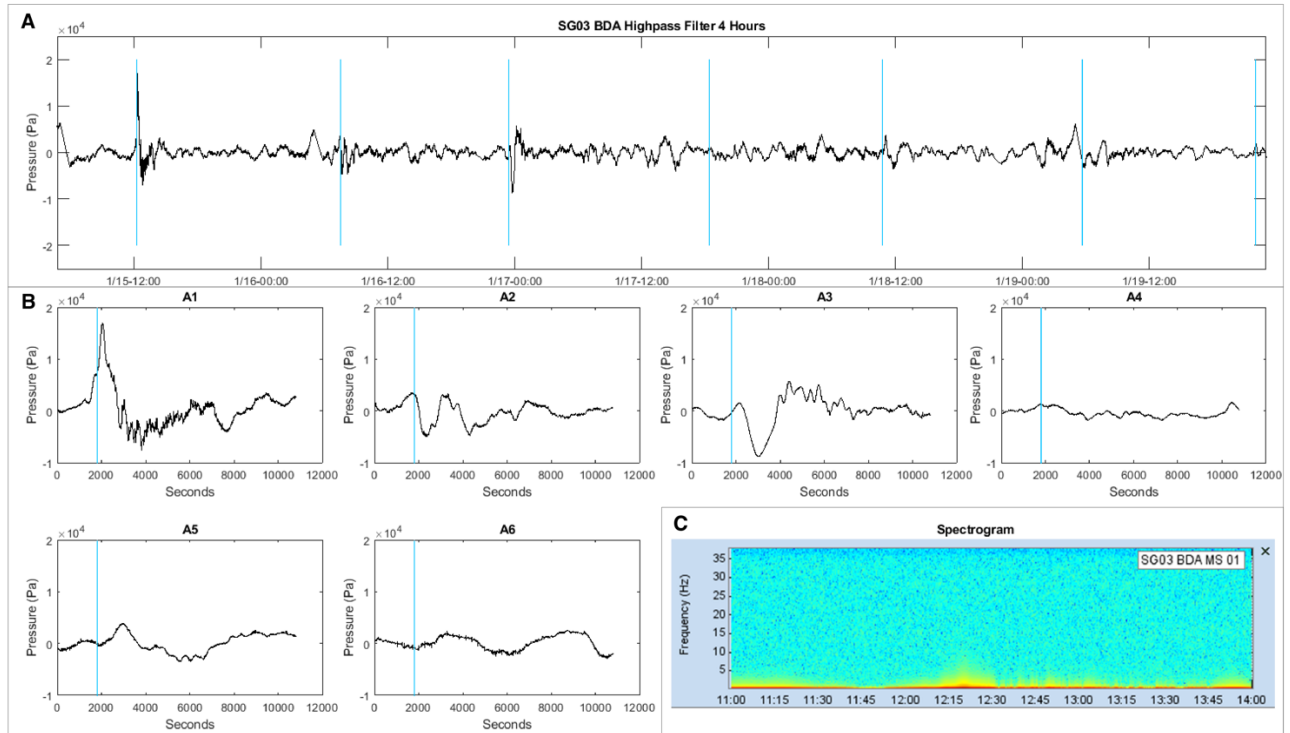
Fig. S20. Regional data processing from Singapore.
(**A**) Details of the signals recorded in Singapore on the absolute pressure channel of one of the MB2005 sensors that make up the Singapore array. In the top panel the BDA absolute pressure channel is highpass filtered above 4 hours to remove diurnal and other long term trends. The expected arrival times of the direct arrivals (A1, A3, A5, A7) are plotted along with the antipodal arrivals (A2, A4, A6) plotted in blue. Below this, in (**B**), are the detailed plots showing the waveform for each of the arrivals from A1-A6. Note that A4 and A6 are not interpreted to have been recorded at this time. In the final panel (**C**) is a spectrogram of the A1 arrival illustrating that there was no signal present in the audio range for this location; no energy was present above 5 Hz.
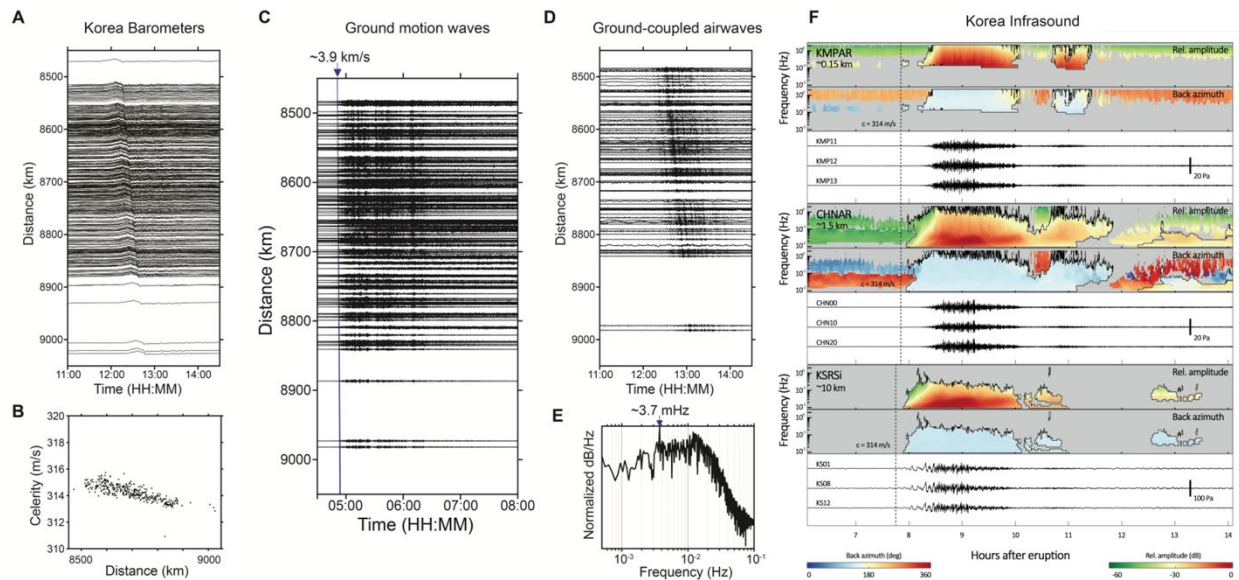
Fig. S21. Regional data processing from Korea.
(**A**) Barometric signals and (**B**) celerity at different epicentral distances. The pressure pulse first arrived at the closest site (~8470 km) at ~11:43:40 UTC and propagated from the eruption with an average celerity of 314 m/s, and is considered a Lamb wave. (**C** and **D**) Seismic recordings at different epicentral distances and (**E**) the power spectral density of air-to-ground-coupled waves. After the direct ground-wave propagating with ~3.9 km/s, strong distinct signals are observed which indicate other wave phases and subsequent explosions. Seismograms also record the air-to-ground-coupled waves having (**E**) a peak frequency of ~3.7 mHz, and the signals are filtered through 0.0005 – 0.1 Hz. (**F**) PMCC detection results and infrasound waveforms recorded at arrays in Korea. Two upper panels for each array display the color-coded relative amplitude and back azimuth of the detections on time–frequency diagrams. Detection results associated with the eruption are bounded with black lines. Vertical dotted lines indicate a celerity of 0.314 km/s, corresponding to the arrival of Lamb waves.
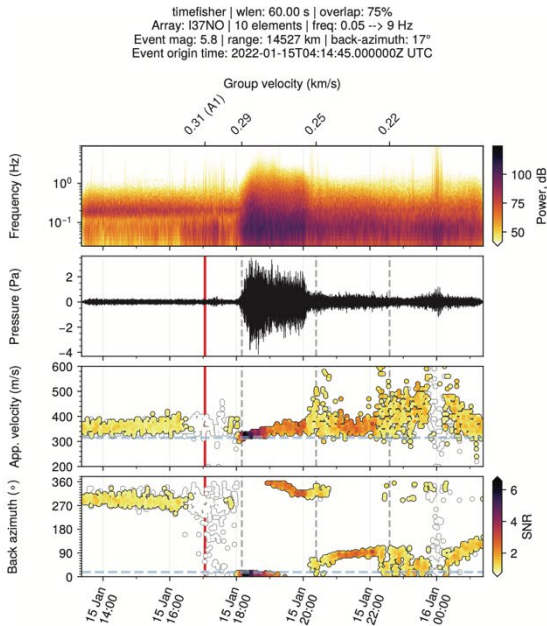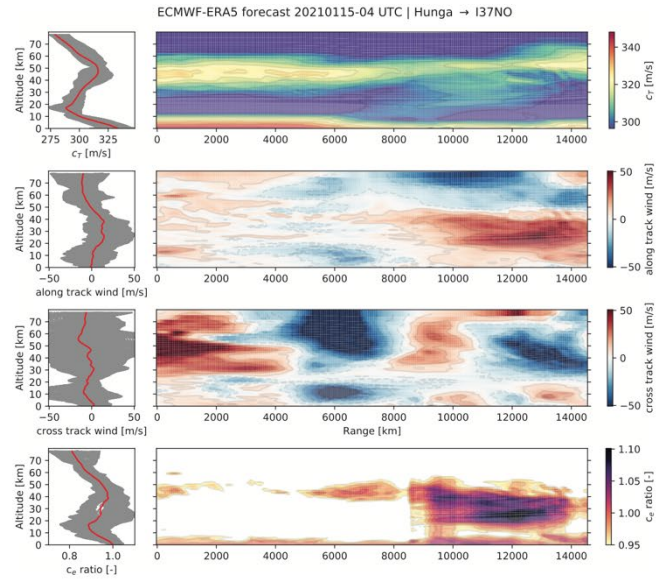
Fig. S22. Backazimuth deviation.
(**A**) Array processing results at IMS infrasound array IS37 at Bardufoss, Norway. The red vertical line highlights A1 arrival time with a velocity of 0.31 km/s; the dashed line represents arrival time for infrasound celerities of 0.29 and 0.25 km/s. For IS37, the infrasound celerity lines up to approximately 0.29 km/s. (**B**) Adiabatic sound speed, along-track, crosswind and effective sound speed as a function of altitude for the path from Hunga volcano to IS37. These parameters were retrieved using ECMWF ERA5 model data.
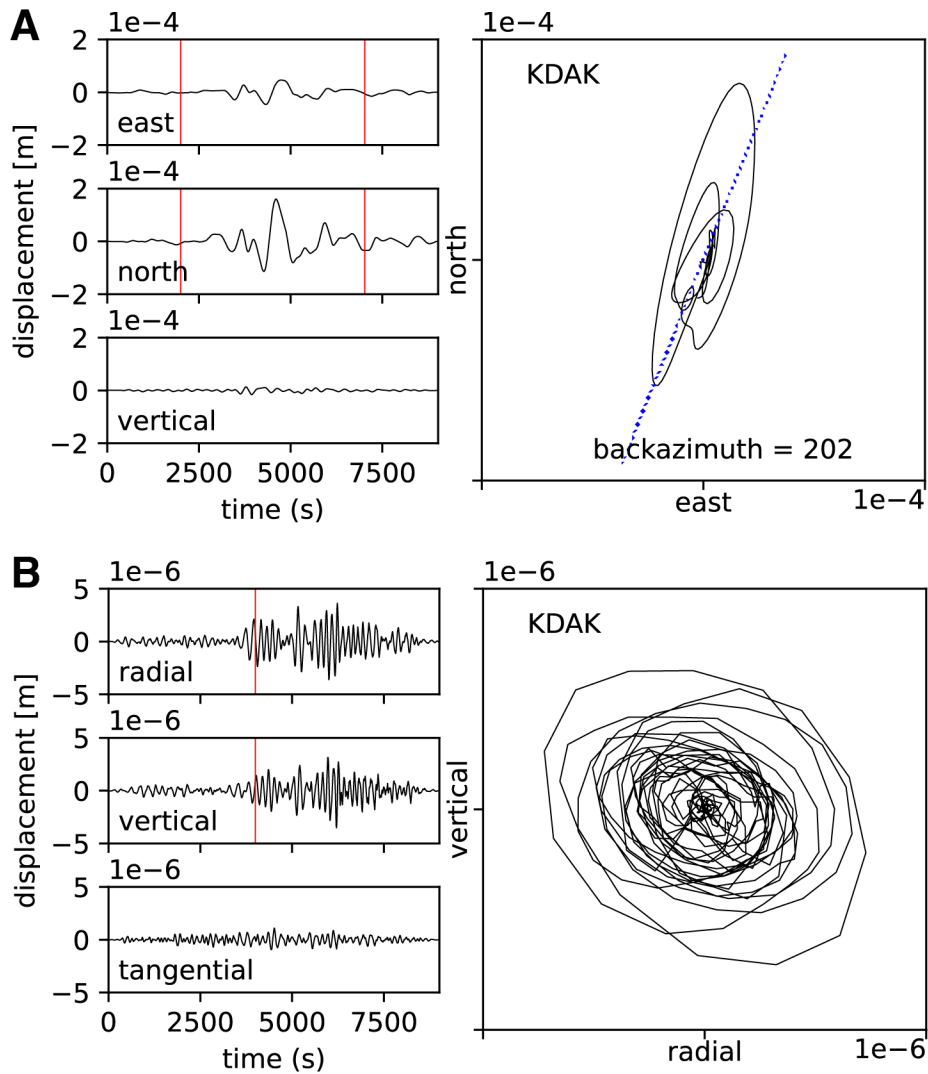
Fig. S23. Seismic displacement and particle motion.
(**A**) (left) Displacement waveforms for station KDAK at Kodiak, Alaska (USA) located approximately 8900 km from the eruption. The red lines denote the window used for the horizontal particle motion plot (right). The dotted blue represents the expected back azimuth from station to source. Data have been detrended and filtered from 0.0005 to 0.005 Hz. (**B**) (left) Displacement waveforms for station KDAK at Kodiak, Alaska located approximately 8900 km from the eruption. The red lines denote the window used for the radial/vertical particle motion plot (right). Data have been detrended and filtered from 0.005 to 0.05 Hz. The particle motion is elliptical, indicating Rayleigh waves.
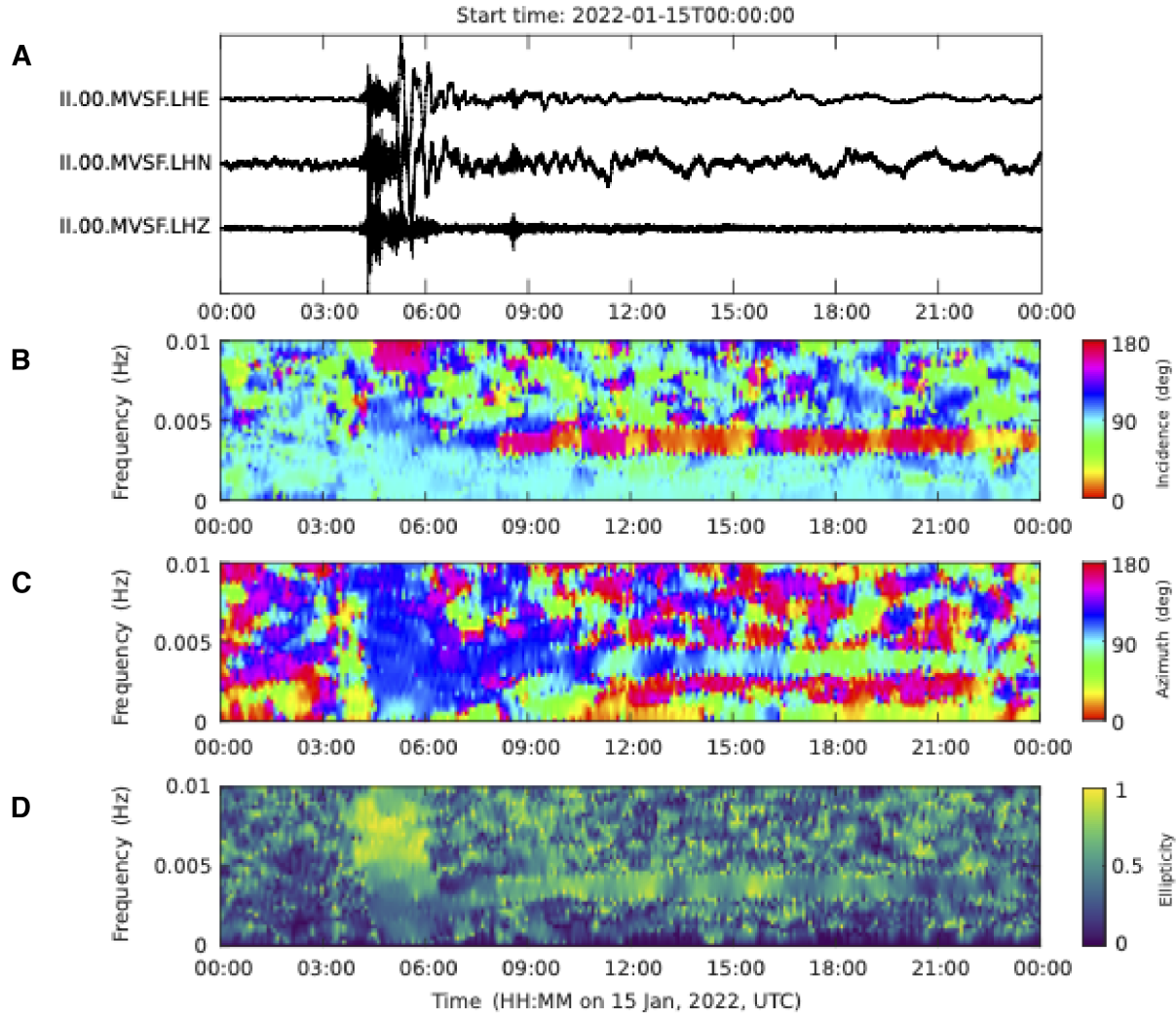
Fig. S24. Seismic polarization at MSVF.
(**A**) Three-component seismogram from station MSVF at Fiji. Low frequency coupling of Lamb wave arrivals is evident on the horizontal components LHN and LHE. (**B-D**) Time-frequency polarization properties of the three-component wavefield at MSVF, including incidence angle, azimuth, and ellipticity. Incidence angle and azimuth have an inherent 180 degree ambiguity and are plotted with a circular colormap between 0 and 180 degrees. Backazimuth to Hunga from station MSVF is 115.28 degrees. Incidence angle is defined as in (*76*) with 0 and 180 degrees representing upward and downward, respectively. The striped pattern in the incidence angle plot beginning at approximately 8:00 UTC for a frequency of roughly 0.0037 Hz is the Solid Earth normal mode $_0S_{29}$ and the incidence angle values indicate it is largest on the vertical component.
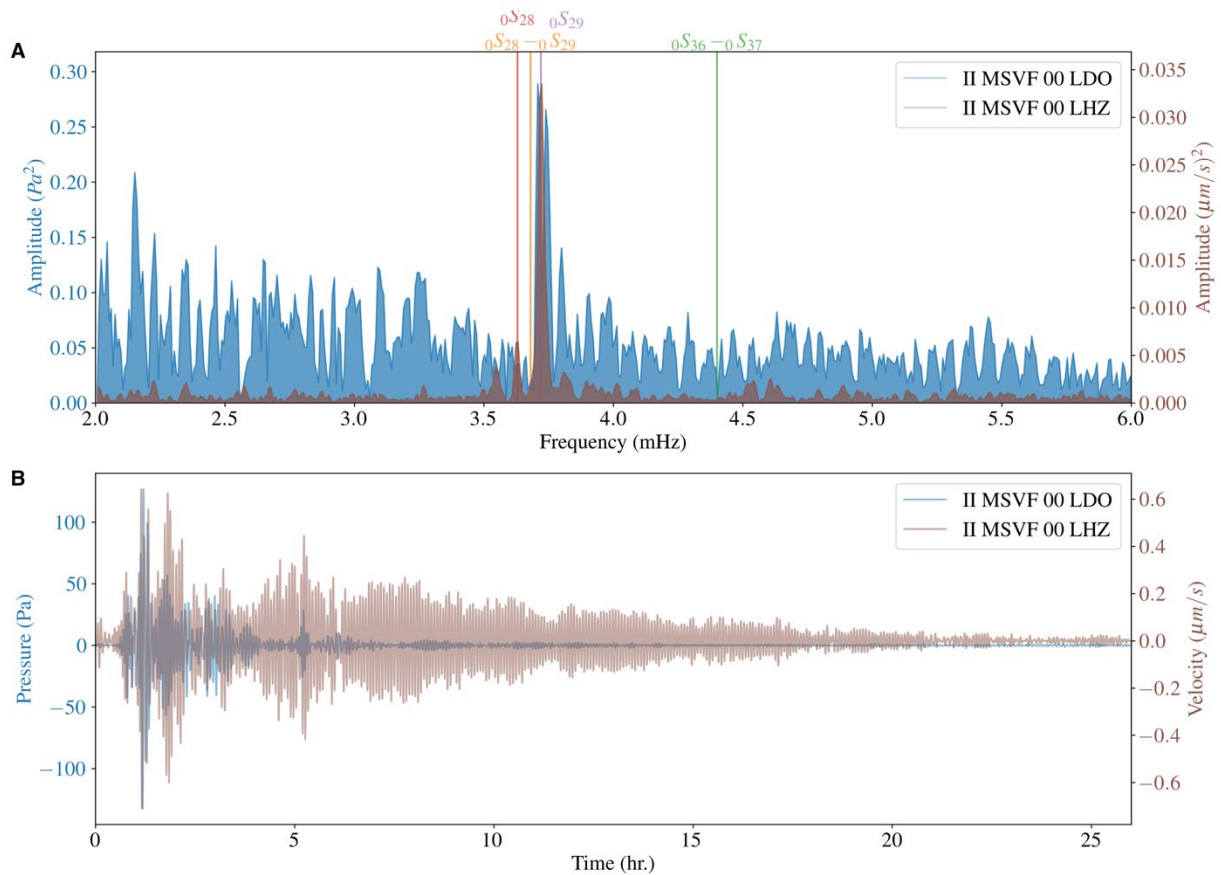
Fig. S25. Pressure and seismic at MSVF.
(**A**) Time-series of pressure (blue) and vertical seismic (red) recorded at station MSVF (Monasavu, Fiji) located 755 km from the Hunga eruption. All traces have been bandpass filtered between 2.5 and 5 mHz and pressure signals begin to be recorded beginning roughly 36 minutes after the eruption. (**B**) Raw (not bandpass filtered) spectra of data plotted in (A). For reference, we include the frequencies of solid Earth normal modes $_0S_{28}$ (3.63 mHz) and $_0S_{29}$ (3.72 mHz) as estimated by the preliminary reference Earth model (PREM; (*77*)) as well as the atmospheric fundamental mode ($_0S_{28}$-$_0S_{29}$; 3.68 mHz) and first harmonic ($_0S_{36}$-$_0S_{37}$; 4.4 mHz) from (*78*).
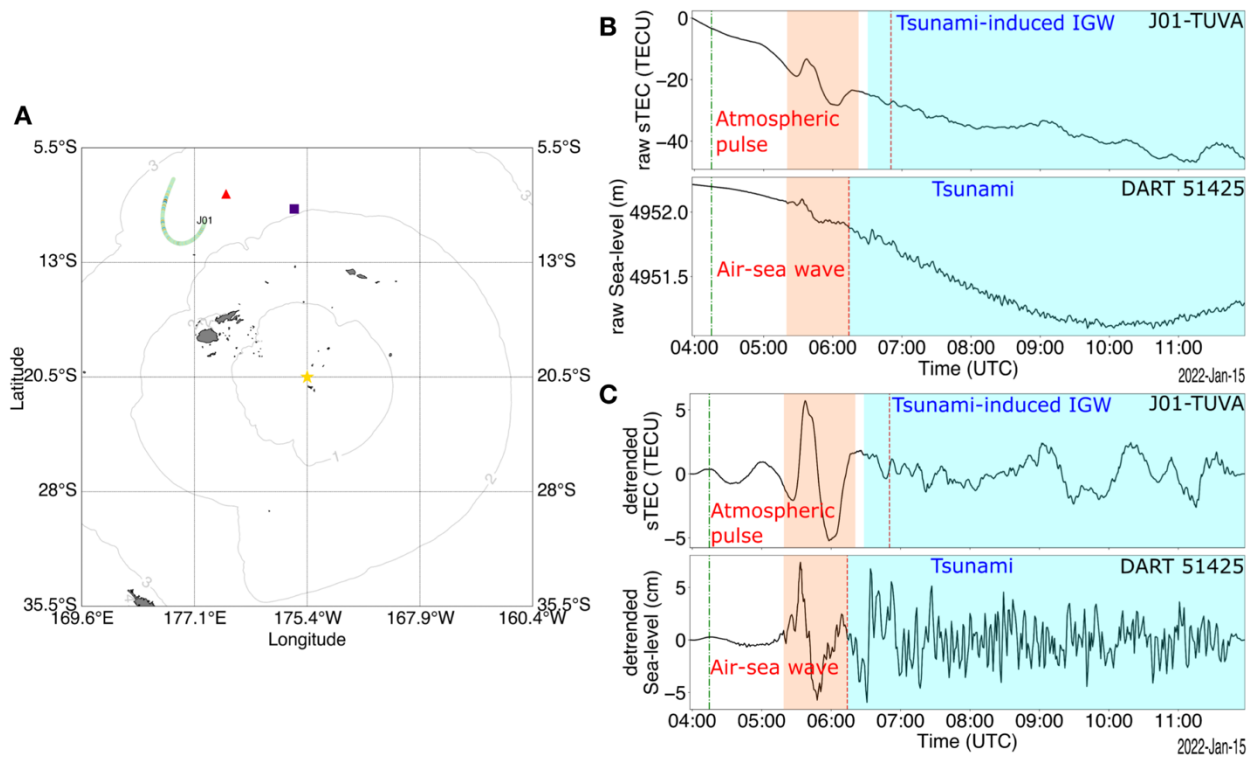
Fig. S26. Ionospheric signature of the atmospheric pulse and tsunami wave.
(**A**) Location map with ionospheric pierce points (IPPs) for the GNSS link G-III (green), the Hunga volcano location (yellow star), GNSS station TUVA (red triangle) and buoy B-I (NDBC/NOAA DART 51425, indigo square). The gray isocontours on the map mark the theoretical travel times in hours for a tsunami wave triggered at the volcano location using the Simple Long Ocean Wave Model (SLOWMO) tool (http://slowmo.sourceforge.net/) and ETOPO1 (1-minute global relief model) as bathymetry model (*79*). Panels (**B**) and (**C**) show link G-III (see Fig. 4F), respectively unfiltered and detrended with a degree-10 polynomial. The dashed vertical green lines at 04:14:45 UTC mark the eruption time and the dashed vertical red lines mark the tsunami arrival times calculated at the measurement points using the map in panel (A).
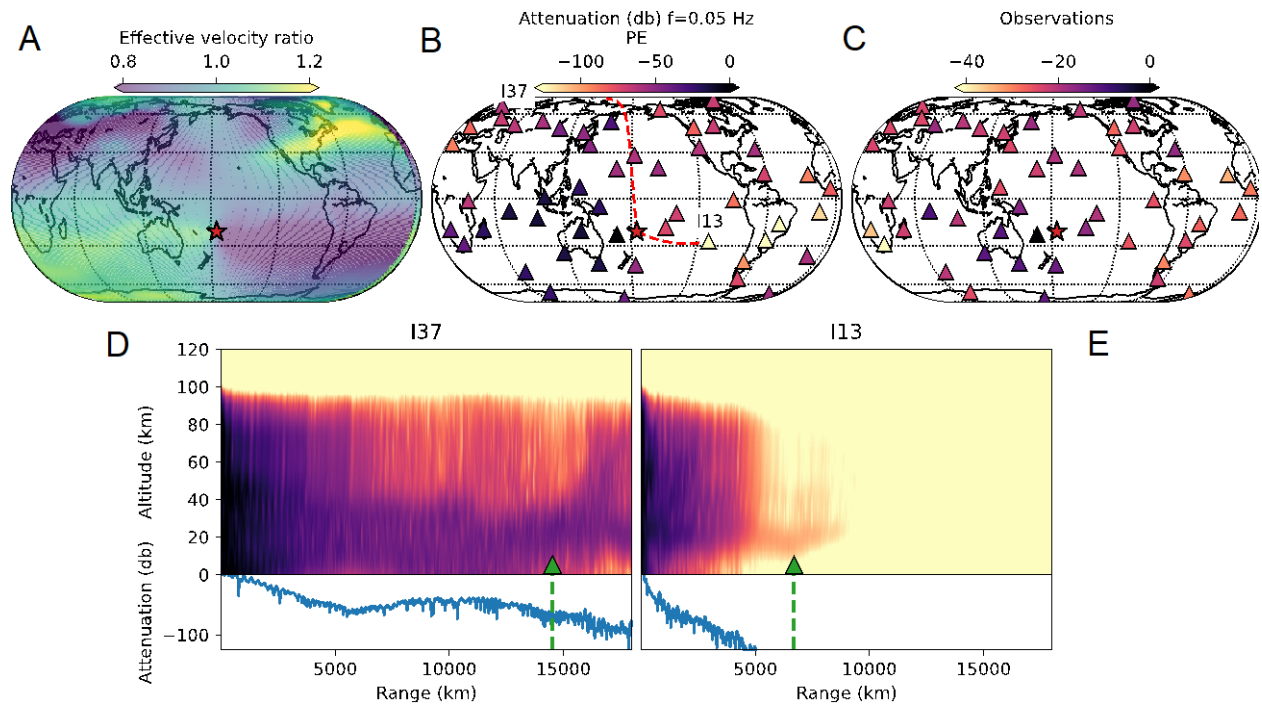
Fig. S27. Comparison between predicted and observed infrasound amplitudes.
(**A**) Effective velocity ratio between averaged ECMWF stratospheric winds (45-55 km altitude) and the ground. Arrows indicate the averaged wind direction between 45 to 55 km altitude. (**B**) PE attenuation predictions (db relative to station IS22) at 0.05 Hz for each IMS station. (**C**) observed attenuation (in db) between 0.047 and 0.053 Hz for selected IMS stations. Note that color scales for panels (B) and (C) are different. Observed amplitudes are normalized with the predicted or observed amplitudes at station IS22. Bottom, predicted TL (Transmission Loss) cross sections towards (**D**) IS37 and (**E**) IS13. Bottom blue curves show ground TLs.
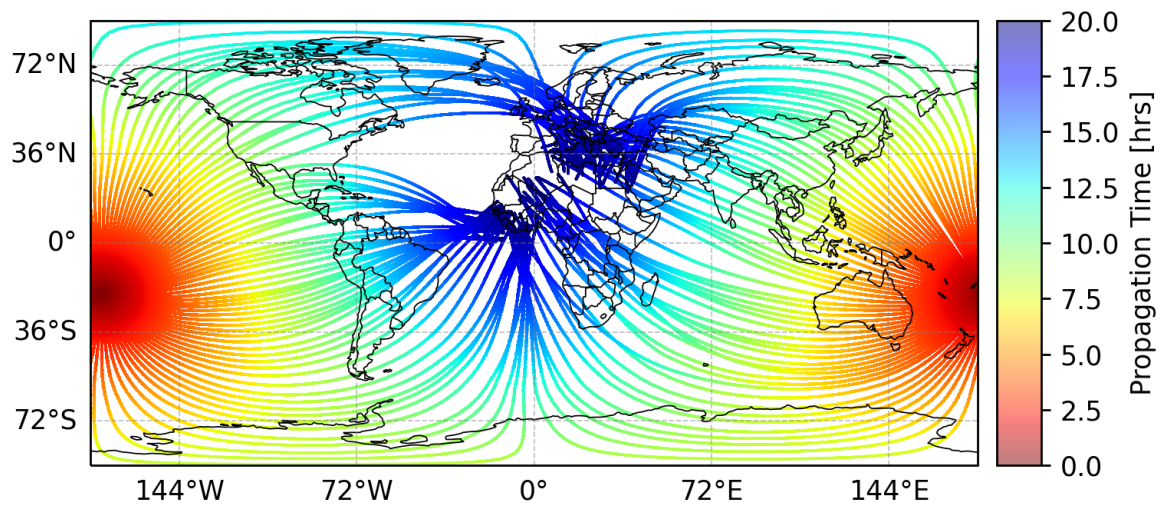
Fig. S28. Global propagation paths.
Global-scale infrasonic propagation paths computed using ray-tracing analysis for a single inclination of 15° relative to the ground surface and an azimuthal resolution of 3° during the first 20 hours after the eruption.
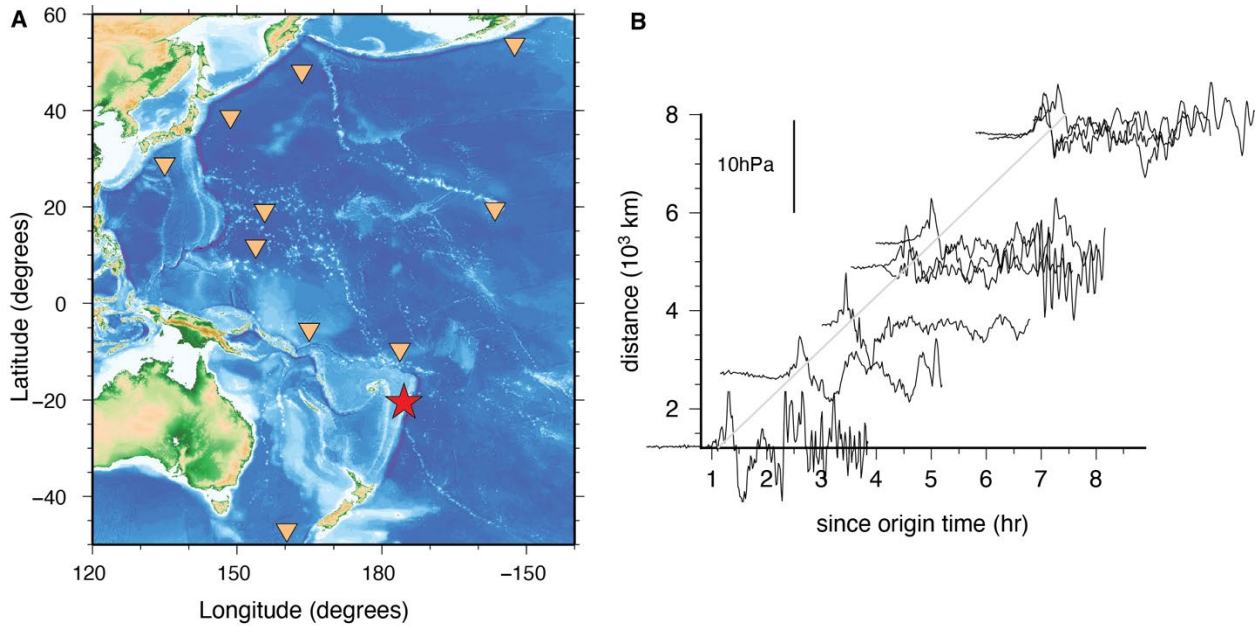
Fig. S29. Tsunamimeter amplitudes.
(**A**) Locations of Hunga eruption (red star) and tide-gauges (orange inverted triangles). We used 10 tsunami detection sensors installed at the deep ocean bottom for tsunami monitoring by NOAA. (**B**) Recorded pressure at deep ocean tsunamimeters in (A). The amplitude of the leading pressure pulse exceeds 6 hPa at a few stations and the average of the peak amplitude is larger than 4 hPa, these numbers are much larger than the values of subaerial pressure sensors. The best fit propagation speed is 298 m/s.
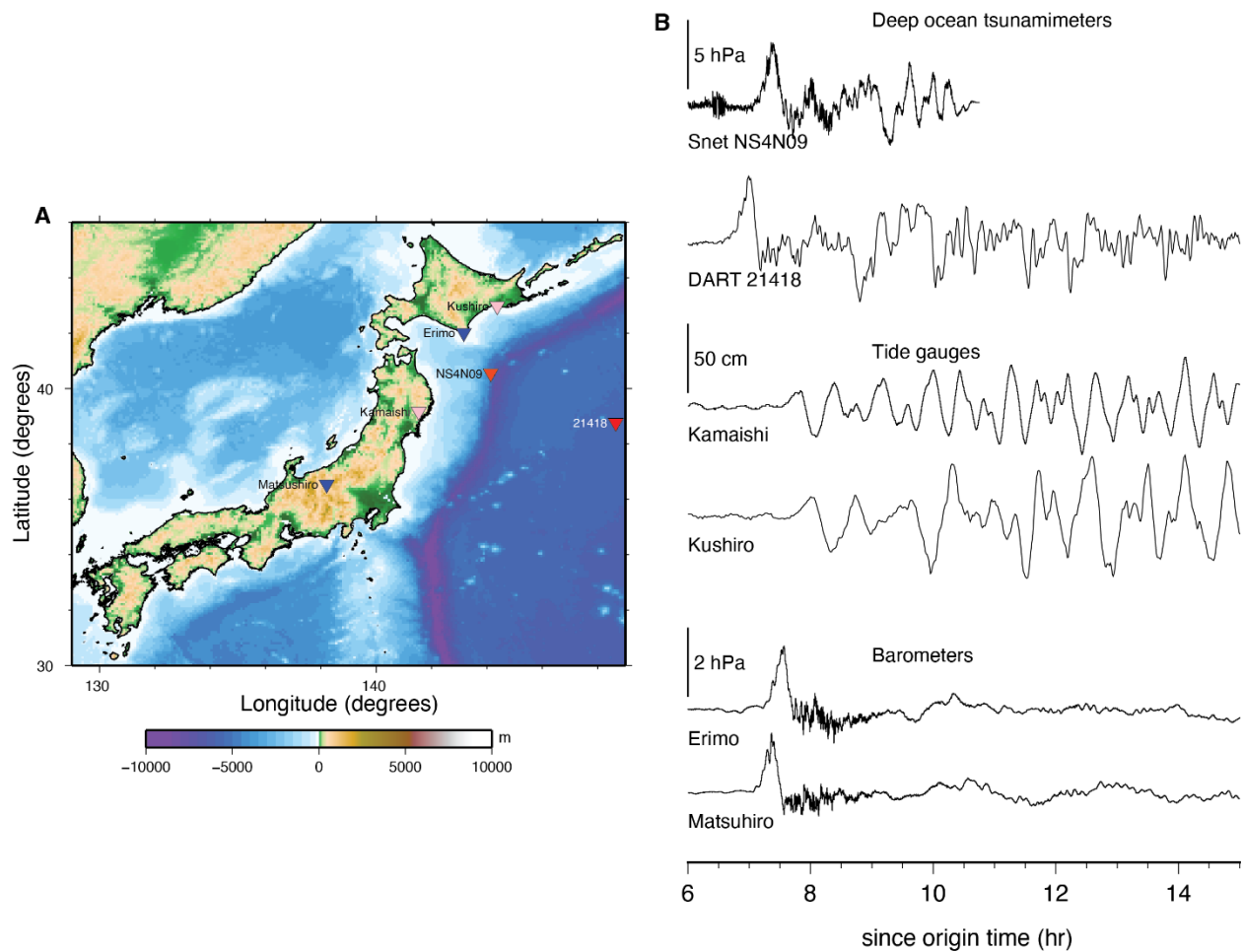
Fig. S30. Pressure records.
(**A**) Locations of pressure sensors. Two deep ocean tsunamimeters are indicated by red inverted triangles, two coastal tide gauges by pink and two barometers by blue. NS4N09 is one of the S-net stations, a seismic and tsunami observation network, which consists of more than 70 cabled nodes of seismic and tsunami sensors. 21418 is a DART station globally distributed for tsunami monitoring by NOAA. (**B**) Pressure records at the stations in Figure (A). Top two records (deep ocean tsunamimeters) and bottom two records (barometers) both have a leading pressure pulse with a similar shape but note that the amplitude of tsunamimeters are two times larger. The tide gauge records (middle two) start without a leading pressure pulse signal, but they gradually grow after the pressure pulse.

Table S1. Infrasound and seismo-acoustic events on 15 January 2022.
Events within a circle of 1 degree around Hunga [20.55°S, 175.39°W] on 15 January 2022 (00:00-12:00 UTC), from the Reviewed Event Bulletin (REB) of the CTBTO International Data Centre (IDC). The table includes both pure infrasound (i.e., based on infrasound detections only) as well as seismo-acoustic events (i.e., formed using at least one P-, S- or T-phase arrival). "Ndef" denotes the number of detections (phases) contributing to the origin time (OT) and location. Magnitude estimates are based on those or fewer detections, resulting in a varying uncertainty of the estimates (0.1-0.3, depth fixed at 0 km). Event details can be found in the Bulletin of the International Seismological Centre (ISC, *80*), which additionally lists moment-magnitude estimates of M_w 5.7-5.8 for the main seismic event. USGS reports a 5.8 Ms_20 magnitude main seismic event with OT 04:14:45 UTC (surface wave magnitude, 20 sec period, https://earthquake.usgs.gov/earthquakes/eventpage/us7000gc8r/origin/detail).

Origin time (UTC)	Latitude	Longitude	Ndef	Event ID REB	Event ID ISC Bulletin	Magnitude	# IMS stations (S, H, I)
03:46:54.92	-21.0082	-175.2190	4	21640504	621831266		4 I
04:06:13.09	-20.6193	-175.4008	17	21650197	621831268	mb 3.9, ML 3.4	8 S 9 I
04:07:49.27	-20.7264	-175.5681	13	21637152	621831269	mb 4.1, ML 3.4	13 S
04:12:54.37	-20.6195	-175.9679	17	21638013	621831270	mb 4.1, ML 3.2	17 S 3 H
04:14:59.70	-20.4995	-175.6472	41	21637158	621831271	mb 4.2, ML 3.5, Ms 5.3	22 S 4 H 21 I
04:30:07.79	-20.7049	-175.7561	41	21638050	621831275		53 I
04:36:51.83	-21.1207	-175.4715	15	21638886	621831279	mb 4.3	13 S
04:40:31.45	-20.6967	-175.2089	16	21637199	621831280	mb 4.2, ML 3.7	16 S
04:49:54.03	-20.9481	-175.1143	4	21650212	621831283	mb 3.8	4 S
05:30:14.65	-20.7291	-175.7462	11	21637293	621831290	mb 4.1, Ms 4.8	22 S 1 H
05:55:22.79	-19.9107	-175.3489	7	21637405	621831293	mb 4.0	7 S
06:06:01.62	-20.1102	-175.8289	8	21637455	621831295	mb 4.0, Ms 4.4	11 S
08:31:38.36	-20.8138	-176.1676	20	21689911	621831306		2 H 20 I

Table S2. Sources for peak-to-peak amplitude values plotted in Fig. 2F. See Data S7 for Hunga 2022 values

Event	Reference
US-15MT	(*13*), Table 3
USSR-57MT	(*13*), Table 3
Beirut	(*81*), Table 2
Krakatau	(*11*)
Mount St. Helens	(*13*), Tables 1 & 2
Bezymianny	(*82*), p.104
Chelyabinsk	(*83*), Supp. Table 1

Table S3. Sources for instrumentally recorded signal period values plotted in Fig. 3F.

Event / Source Type	Min. Freq. (Hz)	Max. Freq. (Hz)	References
Volcanoes			
Krakatau 1883[1]	7.0×10^{-5}	8.3×10^{-4}	(*11*)
Taal 1911[1]	1.9×10^{-4}	3.3×10^{-3}	(*84*)
Bezymianny 1956[1]	8.0×10^{-4}	3.3×10^{-3}	(*82*)
Agung 1963	7.1×10^{-3}	2.9×10^{-2}	(*85*)
Mount St. Helens 1980	9.2×10^{-4} (far-field) 2.8×10^{-4} (near-field)	0.1	(*13,86*)
Pinatubo 1991	1.2×10^{-3}	0.1	(*52*)
International Monitoring System Catalog, 2002-2009	5.6×10^{-3}	5	(*87*)
Atmospheric Nuclear Tests			
USSR and US Tests (1950s and 60s)	1.4×10^{-3}	0.67	(*15,17*)
Bolides			
Tunguska 1908	2.4×10^{-3}	3.3×10^{-2}	(*88*)
Chelyabinsk 2013	1.1×10^{-2}	5	(*83*)
US Catalog, 1960-1974	1.9×10^{-2}	0.4	(*56*)

[1] - Signal frequencies estimated from digitized figures of barograms from original reference

Table S4. Summary table for regional networks. (separate .xlsx file)

Table S5. Predicted arrival characteristics at I37NO using spherical geometry ray tracing.

Celerity	Back Azimuth
256 m/s	-21.4°
250 m/s	-26.2°
248 m/s	-26.6°
244 m/s	-31.5°
242 m/s	-33.0°
242 m/s	-30.5°

References and Notes

1. The name of the volcano is "Hunga," not "Hunga Tonga." "Hunga" refers to the entire volcano, rather than the islands. "Hunga Tonga" refers specifically to the most southwestern of the two islands.

2. R. G. Vaughan, P. W. Webley, Satellite observations of a surtseyan eruption: Hunga Ha'apai, Tonga. *J. Volcanol. Geotherm. Res.* **198**, 177–186 (2010). doi:10.1016/j.jvolgeores.2010.08.017

3. Materials and methods and data and network citations are available as supplementary materials.

4. E. E. Gossard, W. H. Hooke, *Waves in the Atmosphere: Atmospheric Infrasound and Gravity Waves—Their Generation and Propagation* (Elsevier, 1975).

5. K. C. Yeh, C. H. Liu, Acoustic-gravity waves in the upper atmosphere. *Rev. Geophys.* **12**, 193–216 (1974). [doi:10.1029/RG012i002p00193](doi:10.1029/RG012i002p00193)

6. H. Lamb, On atmospheric oscillations. *Proc. R. Soc. London Ser. A* **84**, 551–572 (1911). doi:10.1098/rspa.1911.0008

7. F. P. Bretherton, Lamb waves in a nearly isothermal atmosphere. *Q. J. R. Meteorol. Soc.* **95**, 754–757 (1969). [doi:10.1002/qj.49709540608](doi:10.1002/qj.49709540608)

8. D. Harkrider, F. Press, The Krakatoa air-sea waves: An example of pulse propagation in coupled systems. *Geophys. J. Int.* **13**, 149–159 (1967). [doi:10.1111/j.1365-246X.1967.tb02150.x](doi:10.1111/j.1365-246X.1967.tb02150.x)

9. A. D. Pierce, J. W. Posey, Theory and propagation of Lamb's atmospheric edge mode from nuclear explosions. *Geophys. J. R. Astron. Soc.* **26**, 341–368 (1971). [doi:10.1111/j.1365-246X.1971.tb03406.x](doi:10.1111/j.1365-246X.1971.tb03406.x)

10. R. Matoza, D. Fee, D. Green, P. Mialle, "Volcano infrasound and the International Monitoring System" in *Infrasound Monitoring for Atmospheric Studies: Challenges in Middle Atmosphere Dynamics and Societal Benefits*, A. Le Pichon, E. Blanc, A. Hauchecorne, Eds. (Springer, Cham, 2019), pp. 1023–1077.

11. R. H. Scott, I. Note on a series of barometrical disturbances which passed over Europe between the 27th and the 31st of August, 1883. *Proc. R. Soc. London* **36**, 139–143 (1883). doi:10.1098/rspl.1883.0087

12. R. H. Strachey, "On the air waves and sounds caused by the eruption of Krakatoa in August 1883" in *The Eruption of Krakatoa and Subsequent Phenomena*, Report of the Krakatoa Committee of the Royal Society, G. J. Symons, Ed. (Trübner and Co., 1888).

13. J. W. Reed, Air pressure wave from Mount St. Helens eruptions. *J. Geophys. Res.* **92**, 11979–11992 (1987). [doi:10.1029/JD092iD10p11979](doi:10.1029/JD092iD10p11979)

14. J. W. Posey, A. D. Pierce, Estimation of nuclear explosion energies from microbarograph records. *Nature* **232**, 253–253 (1971). [doi:10.1038/232253a0](doi:10.1038/232253a0) Medline

15. G. B. Olmsted, "Detection of airborne low-frequency sound from nuclear explosions," United States Air Force, Office for Atomic Energy, Operation Castle Report WT-931 (1955)

16. W. L. Donn, D. M. Shaw, A. C. Hubbard, The microbarographic detection of nuclear explosions. *IEEE Trans. Nucl. Sci.* **10**, 285–296 (1963). [doi:10.1109/TNS.1963.4323271](doi:10.1109/TNS.1963.4323271)

17. A. D. Pierce, C. A. Moo, J. W. Posey, "Generation and propagation of infrasonic waves," Air Force Cambridge Research Laboratories, AFCRL-TR-73-0135 (1973).

18. D. Fee, R. Waxler, J. D. Assink, Y. Gitterman, J. Given, J. Coyne, P. Mialle, M. Garces, D. Drob, D. Kleinert, R. Hofstetter, P. Grenard, Overview of the 2009 and 2011 Sayarim infrasound calibration experiments. *J. Geophys. Res. Atmos.* **118**, 6122–6143 (2013). doi:10.1002/jgrd.50398

19. J. J. Lyons, M. M. Haney, D. Fee, W. G. Wech, C. F. Waythomas, Infrasound from giant bubbles during explosive submarine eruptions. *Nat. Geosci.* **12**, 952–958 (2019). [doi:10.1038/s41561-019-0461-0](doi:10.1038/s41561-019-0461-0)

20. F. Press, D. Harkrider, Propagation of acoustic-gravity waves in the atmosphere. *J. Geophys. Res.* **67**, 3889–3908 (1962). [doi:10.1029/JZ067i010p03889](doi:10.1029/JZ067i010p03889)

21. J. N. Brune, J. E. Nafe, L. E. Alsop, The polar phase shift of surface waves on a sphere. *Bull. Seismol. Soc. Am.* **51**, 247–257 (1961). doi:10.1785/BSSA0510020247

22. J. H. Ansell, Legendre functions, the Hilbert transform and surface waves on a sphere. *Geophys. J. Int.* **32**, 95–117 (1973). [doi:10.1111/j.1365-246X.1973.tb06522.x](doi:10.1111/j.1365-246X.1973.tb06522.x)

23. S. Watada, H. Kanamori, Acoustic resonant oscillations between the atmosphere and the solid earth during the 1991 Mt. Pinatubo eruption. *J. Geophys. Res.* **115**, B12319 (2010). [doi:10.1029/2010JB007747](doi:10.1029/2010JB007747)

24. K. Kato, H. Yamasato, The 2011 eruptive activity of Shinmoedake volcano, Kirishimayama, Kyushu, Japan - Overview of activity and Volcanic Alert Level of the Japan Meteorological Agency. *Earth Planets Space* **65**, 2 (2013). [doi:10.5047/eps.2013.05.009](doi:10.5047/eps.2013.05.009)

25. G. A. Valentine, Damage to structures by pyroclastic flows and surges, inferred from nuclear weapons effects. *J. Volcanol. Geotherm. Res.* **87**, 117–140 (1998). [doi:10.1016/S0377-0273(98)00094-8](doi:10.1016/S0377-0273(98)00094-8)

26. J. Proudman, The effects on the sea of changes in atmospheric pressure. *Geophys. Suppl. Mon. Not. R. Astron. Soc.* **2**, 197–209 (1929). [doi:10.1111/j.1365-246X.1929.tb05408.x](doi:10.1111/j.1365-246X.1929.tb05408.x)

27. A. M. Portas, L. Barnard, C. Scott, R. G. Harrison, The National Eclipse Weather Experiment: Use and evaluation of a citizen science tool for schools outreach. *Philos. Trans. R. Soc. London Ser. A* **374**, 20150223 (2016). doi:10.1098/rsta.2015.0223 Medline

28. E. Calais, S. Symithe, T. Monfret, B. Delouis, A. Lomax, F. Courboulex, J. P. Ampuero, P. E. Lara, Q. Bletery, J. Chèze, F. Peix, A. Deschamps, B. de Lépinay, B. Raimbault, R. Jolivet, S. Paul, S. St Fleur, D. Boisson, Y. Fukushima, Z. Duputel, L. Xu, L. Meng, Citizen seismology helps decipher the 2021 Haiti earthquake. *Science* **376**, 283–287 (2022). doi:10.1126/science.abn1045 Medline

29. M. Beyreuther, R. Barsch, L. Krischer, T. Megies, Y. Behr, J. Wassermann, ObsPy: A Python toolbox for seismology. *Seismol. Res. Lett.* **81**, 530–533 (2010). doi:10.1785/gssrl.81.3.530

30. T. K. Ahern, B. Dost, SEED (Standard for the Exchange of Earthquake Data) Reference Manual, SEED format version 2.4 (Incorporated Research Institutions for Seismology (IRIS), 2012).

31. A. Rohatgi, WebPlotDigitizer (2020); https://automeris.io/WebPlotDigitizer.

32. R. G. Harrison, Pressure anomalies from the January 2022 Hunga Tonga-Hunga Ha'apai eruption. *Weather* **77**, 87–90 (2022). doi:10.1002/wea.4170

33. G. Harrison, Tonga eruption atmospheric pressure wave data, University of Reading Research Data Archive (2022); https://doi.org/10.17864/1947.000354.

34. S. N. Gurbatov, O. V. Rudenko, "Statistical phenomena" in *Nonlinear Acoustics*, M. F. Hamilton, D. T. Blackstock, Eds. (Academic Press, 1998), pp. 377–398.

35. R. L. Parker, PSD: Power Spectra by Sine Multitapers (2014); https://igppweb.ucsd.edu/~parker/Software/.

36. H. Kanamori, J. Mori, D. G. Harkrider, Excitation of atmospheric oscillations by volcanic eruptions. *J. Geophys. Res.* **99**, 21947–21961 (1994). doi:10.1029/94JB01475

37. R. Ware, M. Exner, D. Feng, M. Gorbunov, K. Hardy, B. Herman, Y. Kuo, T. Meehan, W. Melbourne, C. Rocken, W. Schreiner, S. Sokolovskiy, F. Solheim, X. Zou, R. Anthes, S. Businger, K. Trenberth, GPS sounding of the atmosphere from low earth orbit: Preliminary results. *Bull. Am. Meteorol. Soc.* **77**, 19–40 (1996). doi:10.1175/1520-0477(1996)077<0019:GSOTAF>2.0.CO;2

38. R. A. Anthes, Exploring Earth's atmosphere with radio occultation: Contributions to weather, climate and space weather. *Atmos. Meas. Tech.* **4**, 1077–1103 (2011). doi:10.5194/amt-4-1077-2011

39. W. S. Schreiner, J. P. Weiss, R. A. Anthes, J. Braun, V. Chu, J. Fong, D. Hunt, Y. H. Kuo, T. Meehan, W. Serafino, J. Sjoberg, S. Sokolovskiy, E. Talaat, T. K. Wee, Z. Zeng, COSMIC-2 Radio Occultation Constellation: First results. *Geophys. Res. Lett.* **47**, e2019GL086841 (2020). doi:10.1029/2019GL086841

40. N. E. Bowler, An assessment of GNSS radio occultation data produced by Spire. *Q. J. R. Meteorol. Soc.* **146**, 3772–3788 (2020). doi:10.1002/qj.3872

41. G. Blewitt, An automatic editing algorithm for GPS data. *Geophys. Res. Lett.* **17**, 199–202 (1990). doi:10.1029/GL017i003p00199

42. P. J. G. Teunissen, O. Montenbruck, *Springer Handbook of Global Navigation Satellite Systems* (Springer, Cham, 2017).

43. G. Mungov, M. Eblé, R. Bouchard, DART® tsunameter retrospective and real-time data: A reflection on 10 years of processing in support of tsunami research and operations. *Pure Appl. Geophys.* **170**, 1369–1384 (2013). doi:10.1007/s00024-012-0477-5

44. J. Marty, "The IMS infrasound network: Current status and technological developments" in *Infrasound Monitoring for Atmospheric Studies: Challenges in Middle Atmosphere Dynamics and Societal Benefits*, A. Le Pichon, E. Blanc, A. Hauchecorne, Eds. (Springer, Cham, 2019), pp. 3–62.

45. P. Mialle, D. Brown, N. Arora, colleagues from IDC, "Advances in operational processing at the International Data Centre" in *Infrasound Monitoring for Atmospheric Studies: Challenges in Middle Atmosphere Dynamics and Societal Benefits*, A. Le Pichon, E. Blanc, A. Hauchecorne, Eds. (Springer, Cham, 2019), pp. 209–248.

46. L. G. Evers, "The inaudible symphony: On the detection and source identification of atmospheric infrasound," thesis, TU Delft (2008).

47. Y. Cansi, An automatic seismic event processing for detection and location: The PMCC method. *Geophys. Res. Lett.* **22**, 1021–1024 (1995). doi:10.1029/95GL00468

48. K. Nishida, N. Kobayashi, Y. Fukao, Background Lamb waves in the Earth's atmosphere. *Geophys. J. Int.* **196**, 312–316 (2014). doi:10.1093/gji/ggt413

49. T. Gabrielson, Krakatoa and the Royal Society: The Krakatoa explosion of 1883. *Acoust. Today* **6**, 14–19 (2010). doi:10.1121/1.3467643

50. F. Press, D. Harkrider, Air-sea waves from the explosion of Krakatoa. *Science* **154**, 1325–1327 (1966). doi:10.1126/science.154.3754.1325 Medline

51. W. L. Donn, N. K. Balachandran, Mount St. Helens eruption of 18 May 1980: Air waves and explosive yield. *Science* **213**, 539–541 (1981). doi:10.1126/science.213.4507.539 Medline

52. M. Tahira, M. Nomura, Y. Sawada, K. Kamo, "Infrasonic and acoustic-gravity waves generated by the Mount Pinatubo eruption of June 15, 1991" in *Fire and Mud: Eruptions and Lahars of Mount Pinatubo, Philippines* (US Geological Survey, 1996), pp. 601–614.

53. C. E. Needham, *Blast Waves* (Springer, 2010).

54. D. Fee, R. S. Matoza, An overview of volcano infrasound: From Hawaiian to Plinian, local to global. *J. Volcanol. Geotherm. Res.* **249**, 123–139 (2013). doi:10.1016/j.jvolgeores.2012.09.002

55. G. F. Kinney, K. J. Graham, *Explosive Shocks in Air* (Springer Science & Business Media, 2013).

56. D. O. Revelle, "Historical detection of atmospheric impacts by large bolides using acoustic-gravity waves," Los Alamos National Laboratory, Technical Report LA-UR-95-1263 (1995).

57. M. Ripepe, D. D. Donne, R. Genco, G. Maggio, M. Pistolesi, E. Marchetti, G. Lacanna, G. Ulivieri, P. Poggi, Volcano seismicity and ground deformation unveil the gravity-driven magma discharge dynamics of a volcanic eruption. *Nat. Commun.* **6**, 6998 (2015). doi:10.1038/ncomms7998 Medline

58. J. Capon, Investigation of long-period noise at the large aperture seismic array. *J. Geophys. Res.* **74**, 3182–3194 (1969). doi:10.1029/JB074i012p03182

59. G. G. Sorrells, J. A. McDonald, Z. A. Der, E. Herrin, Earth motion caused by local atmospheric pressure changes. *Geophys. J. R. Astron. Soc.* **26**, 83–98 (1971). doi:10.1111/j.1365-246X.1971.tb03384.x

60. P. W. Rodgers, The response of the horizontal pendulum seismometer to Rayleigh and Love waves, tilt, and free oscillations of the Earth. *Bull. Seismol. Soc. Am.* **58**, 1385–1406 (1968). doi:10.1785/BSSA0580051385

61. R. Raspet, C. J. Hickey, B. Koirala, Corrected tilt calculation for atmospheric pressure-induced seismic noise. *Appl. Sci.* **12**, 1247 (2022). doi:10.3390/app12031247

62. L. M. Rolland, G. Occhipinti, P. Lognonné, A. Loevenbruck, Ionospheric gravity waves detected offshore Hawaii after tsunamis. *Geophys. Res. Lett.* **37**, L17101 (2010). doi:10.1029/2010GL044479

63. R. Waxler, J. D. Assink, "Propagation modeling through realistic atmosphere and benchmarking" in *Infrasound Monitoring for Atmospheric Studies: Challenges in Middle Atmosphere Dynamics and Societal Benefits*, A. Le Pichon, E. Blanc, A. Hauchecorne, Eds. (Springer, Cham, 2019), pp. 509–549.

64. P. Blom, Modeling infrasonic propagation through a spherical atmospheric layer—Analysis of the stratospheric pair. *J. Acoust. Soc. Am.* **145**, 2198–2208 (2019). doi:10.1121/1.5096855 Medline

65. R. Waxler, C. Hetzer, J. Assink, D. Velea, chetzer-ncpa/ncpaprop-release: NCPAprop, version 2.1.0, Zenodo (2021); https://doi.org/10.5281/zenodo.5562713.

66. H. Hersbach, B. Bell, P. Berrisford, G. Biavati, A. Horányi, J. Muñoz Sabater, J. Nicolas, C. Peubey, R. Radu, I. Rozum, D. Schepers, A. Simmons, C. Soci, D. Dee, J.-N. Thépaut, ERA5 hourly data on pressure levels from 1979 to present, Copernicus Climate Change Service (C3S) Climate Data Store (CDS) (2018); https://doi.org/10.24381/cds.bd0915c6.

67. D. P. Drob, J. M. Picone, M. Garcés, Global morphology of infrasound propagation. *J. Geophys. Res.* **108**, 4680 (2003). doi:10.1029/2002JD003307

68. J. M. Picone, A. E. Hedin, D. P. Drob, A. C. Aikin, NRLMSISE-00 empirical model of the atmosphere: Statistical comparisons and scientific issues. *J. Geophys. Res.* **107**, 1468 (2002). doi:10.1029/2002JA009430

69. D. P. Drob, J. T. Emmert, J. W. Meriwether, J. J. Makela, E. Doornbos, M. Conde, G. Hernandez, J. Noto, K. A. Zawdie, S. E. McDonald, J. D. Huba, J. H. Klenzing, An update to the Horizontal Wind Model (HWM): The quiet time thermosphere. *Earth Space Sci.* **2**, 301–319 (2015). doi:10.1002/2014EA000089

70. P. S. M. Smets, J. D. Assink, A. Le Pichon, L. G. Evers, ECMWF SSW forecast evaluation using infrasound. *J. Geophys. Res. Atmos.* **121**, 4637–4650 (2016). doi:10.1002/2015JD024251

71. J. D. Assink, R. Waxler, P. Smets, L. G. Evers, Bidirectional infrasonic ducts associated with sudden stratospheric warming events. *J. Geophys. Res. Atmos.* **119**, 1140–1153 (2014). doi:10.1002/2013JD021062

72. W. L. Donn, The microbarovariograph: A new instrument for measuring minute atmospheric pressure variations. *Trans. Am. Geophys. Union* **39**, 366–368 (1958). doi:10.1029/TR039i002p00353

73. D. G. Harkrider, Theoretical and observed acoustic-gravity waves from explosive sources in the atmosphere. *J. Geophys. Res.* **69**, 5295–5321 (1964). doi:10.1029/JZ069i024p05295

74. S. Shani-Kadmiel, G. Averbuch, P. Smets, J. Assink, L. Evers, The 2010 Haiti earthquake revisited: An acoustic intensity map from remote atmospheric infrasound observations. *Earth Planet. Sci. Lett.* **560**, 116795 (2021). doi:10.1016/j.epsl.2021.116795

75. A. Levshin, L. Ratnikova, J. Berger, Peculiarities of surface-wave propagation across central Eurasia. *Bull. Seismol. Soc. Am.* **82**, 2464–2493 (1992). doi:10.1785/BSSA0820062464

76. M. M. Haney, D. Fee, K. F. McKee, J. J. Lyons, R. S. Matoza, A. G. Wech, G. Tepp, C. Searcy, T. D. Mikesell, Co-eruptive tremor from Bogoslof volcano: Seismic wavefield composition at regional distances. *Bull. Volcanol.* **82**, 18 (2020). [doi:10.1007/s00445-019-1347-0](doi:10.1007/s00445-019-1347-0)

77. A. M. Dziewonski, D. L. Anderson, Preliminary reference Earth model. *Phys. Earth Planet. Inter.* **25**, 297–356 (1981). [doi:10.1016/0031-9201(81)90046-7](doi:10.1016/0031-9201(81)90046-7)

78. P. Lognonné, E. Clévédé, H. Kanamori, Computation of seismograms and atmospheric oscillations by normal-model summation for a spherical earth model with realistic atmosphere. *Geophys. J. Int.* **135**, 388–406 (1998). [doi:10.1046/j.1365-246X.1998.00665.x](doi:10.1046/j.1365-246X.1998.00665.x)

79. C. Amante, B. W. Eakins, ETOPO1: 1 Arc-Minute Global Relief Model: Procedures, Data Sources and Analysis (NOAA Technical Memorandum NESDIS NGDC-24, 2009); https://doi.org/10.7289/V5C8276M.

80. International Seismological Centre, On-line Bulletin (2022); https://doi.org/10.31905/D808B830.

81. C. Pilger, P. Gaebler, P. Hupe, A. C. Kalia, F. M. Schneider, A. Steinberg, H. Sudhaus, L. Ceranna, Yield estimation of the 2020 Beirut explosion using open access waveform and remote sensing data. *Sci. Rep.* **11**, 14144 (2021). [doi:10.1038/s41598-021-93690-y](doi:10.1038/s41598-021-93690-y) Medline

82. G. S. Gorshkov, Gigantic eruption of the volcano Bezymianny. *Bull. Volcanol.* **20**, 77–109 (1959). [doi:10.1007/BF02596572](doi:10.1007/BF02596572)

83. P. G. Brown, J. D. Assink, L. Astiz, R. Blaauw, M. B. Boslough, J. Borovička, N. Brachet, D. Brown, M. Campbell-Brown, L. Ceranna, W. Cooke, C. de Groot-Hedlin, D. P. Drob, W. Edwards, L. G. Evers, M. Garces, J. Gill, M. Hedlin, A. Kingery, G. Laske, A. Le Pichon, P. Mialle, D. E. Moser, A. Saffer, E. Silber, P. Smets, R. E. Spalding, P. Spurný, E. Tagliaferri, D. Uren, R. J. Weryk, R. Whitaker, Z. Krzeminski, A 500-kiloton airburst over Chelyabinsk and an enhanced hazard from small impactors. *Nature* **503**, 238–241 (2013). doi:10.1038/nature12741 Medline

84. M. Saderra Masó, *The Eruption of Taal Volcano, January 30, 1911* (Dept. of the Interior, Weather Bureau, Manila Bureau of Printing, 1911).

85. V. H. Goerke, J. M. Young, R. K. Cook, Infrasonic observations of the May 16, 1963, volcanic explosion on the Island of Bali. *J. Geophys. Res.* **70**, 6017–6022 (1965). [doi:10.1029/JZ070i024p06017](doi:10.1029/JZ070i024p06017)

86. B. A. Bolt, T. Tanimoto, Atmospheric oscillations after the May 18, 1980 eruption of Mount St. Helens. *Eos* **62**, 529–530 (1981). [doi:10.1029/EO062i023p00529](doi:10.1029/EO062i023p00529)

87. A. L. Dabrowa, D. N. Green, A. C. Rust, J. C. Phillips, A global study of volcanic infrasound characteristics and the potential for long-range monitoring. *Earth Planet. Sci. Lett.* **310**, 369–379 (2011). doi:10.1016/j.epsl.2011.08.027

88. H. Wexler, W. A. Hass, Global atmospheric pressure effects of the October 30, 1961, explosion. *J. Geophys. Res.* **67**, 3875–3887 (1962). doi:10.1029/JZ067i010p03875